Check for updates

Revisiting the band gap problem in bulk Co_3O_4 and its isostructural Zn and Al derivatives through the lens of theoretical spectroscopy†

Anneke Dittmer,[ac] Tiago Leyser da Costa Gouveia,[a] Kantharuban Sivalingam,[a] Serena DeBeer, ✶[b] Frank Neese✶[a] and Dimitrios Maganas ✶[a]

In this work, a systematic computational investigation of the optical band gap (BG) problem of Co_3O_4 is carried out on the basis of the embedded cluster approach in combination with a series of particle/hole and wavefunction-based approaches. A total number of three experimental band gap energies for the bulk Co_3O_4 have been reported in the literature, the nature of which have remained controversial. This work will show that accurately describing the excited states and rationalizing these experimental band gaps require explicit treatment and analysis of strong electron correlation effects. These correlation effects enable low-energy optical excitations to emerge from both 'neutral' and 'ionic' antiferromagnetic configurations, depending on how the electronic structure reorganizes across the coupled high-spin tetrahedral Co(II) (site A) and low-spin octahedral Co(III) (site B) centers. To disentangle the contributions from these two distinct sites, this work introduces reference systems, $Al_2Co(II)O_4$ and $Co(III)_2ZnO_4$, which isolate the Co(II) and Co(II) sites, respectively. Tackling such a complex excited state problem requires going beyond density functional theory (DFT) particle/hole approaches and employing a range of single and multi-reference wavefunction based methods. In particular, complete active space configuration interaction self-consistent field (CASSCF) and its approximate CI variants in conjunction with 2nd order N-electron valence perturbation theory (NEVPT2) provide access to an accurate prediction of all three experimentally observed BG energies in Co_3O_4. Our calculations are consistent with the notion that the lowest energy band gap corresponds to the ligand field (LF) type of transitions within the local tetrahedral Co(II) centers. Furthermore, the calculations predict that the middle energy band gap is a mixture of LF transitions at site A and metal-to-metal charge transfer (MMCT) transition across A–A' and A–B/B–A' pairs. These transitions give rise to Co(I) and Co(III) configurations at site A, deviating from the original Co(II) based configurations. This intermediate band is assigned to the actual experimentally observed optical band gap of Co_3O_4. Finally, the highest energy band gap is again a mixture of LF transitions at site A and ligand-to-metal charge transfer (LMCT), involving O 2p → Co(II)-3d transitions, with our calculations also indicating some contributions from other MMCT states. Hence, this later energy band corresponds to the actual semiconducting band gap that defines the semiconductor properties of Co_3O_4.

I. Introduction

The spinel-structured cobalt oxide Co_3O_4 exhibits intriguing electrochemical and photochemical properties that are of interest for numerous applications in the increasingly important field of sustainable energy conversion. In particular, in the field of heterogeneous catalysis, cobalt-based spinel oxides reveal promising results for various oxidation reactions, such as selective CO oxidation,[1–7] volatile organic compound (VOC) combustion,[7–9] and alcohol oxidation,[10–13] as well as oxygen reduction, oxygen evolution reactions (OERs),[14–20] and hydrogen evolution reactions (HERs).[20–23] The latter and the wide availability of Co_3O_4 have made this material a hopeful prospect for application areas, such as fuel cells, water splitting, and artificial photosynthesis.[16–23] Furthermore, alloys containing Co_3O_4 have been the subject of various investigations concerning photovoltaic applications.[24–28] In this regard, of particular

[a] *Max-Planck-Institut für Kohlenforschung, Kaiser-Wilhelm-Platz 1, D-45470 Mülheim an der Ruhr, Germany. E-mail: dimitrios.manganas@kofo.mpg.de*

[b] *Max-Planck Institute for Chemical Energy Conversion, Stiftstrasse 34-36, D-45470 Mülheim an der Ruhr, Germany*

[c] *FACCTs GmbH, Rolandstrasse 67, D-50677 Köln, Germany*

† Electronic supplementary information (ESI) available: Literature and analysis tables together with discussions regarding the impact of electron correlation on the excited states and the magnetic ground state of Co_3O_4 along with representative inputs are provided. See DOI: https://doi.org/10.1039/d5cp01735a

This journal is © the Owner Societies 2025

Phys. Chem. Chem. Phys., 2025, **27**, 17225–17244 | **17225**

interest is that the semiconducting Co_3O_4 has various optical excitations that cover a large portion of the solar spectrum.[24,29] The optical band gap of a material, which is its first non-dark excited state,[30] is usually the associated decisive fundamental property.

The *status quo* of most experimental and theoretical band gap studies indicates that Co_3O_4 actually has two band gaps, not one. One at about 1.5 eV and a more intense one at about 2.1 eV.[26,29,31–50] Some experimental studies suggest an even higher number of band gaps[29,34,42,43] or at least lower-lying absorption bands that could direct towards another band gap.[29,33,34,36–38,51–57] Furthermore, there are still ambiguities regarding the actual origin and character of these band gaps.[29]

The concept of optical band gaps is not only essential to understand the photochemical behavior but also to gain a broader knowledge of the general electronic structure of Co_3O_4 and, thus, the prospect of understanding the general physical, chemical, and especially catalytic behavior of Co_3O_4 concerning the previously listed application possibilities.[29] In this context, it is of interest to comprehend the role of the different cobalt sites in the system since Co_3O_4 contains both tetrahedral $Co(II)$ sites and distorted octahedral $Co(III)$ sites in a $1:2$ ratio. Moreover, the $Co(II)$ sites with a local high-spin electron configuration $e^4 t^3$ exhibit weak antiferromagnetic coupling, which on the basis of the experimental Néel temperatures and mean-field theory corresponds to $J \sim 2$–5 cm^{-1},[58,59] while the $Co(III)$ sites with a local low spin configuration $t_{2g}^6 e_g^0$ are usually considered diamagnetic.[29,60] Although the degree of antiferromagnetic coupling between the interacting Co centers is rather small, accurately probing the spin and oxidation states in the Co_3O_4 spinel catalyst and its synthetic derivatives[61,62] – in correlation with spectroscopic observables – remains a fundamentally challenging task.[12,63–66]

It should be mentioned that the magnetic structure of Co_3O_4 has been a subject of interest, with several studies exploring the possibility of non-collinear magnetic ordering at low temperatures, particularly at interfaces or in related systems, as evidenced by experimental and theoretical investigations.[67,68] This non-collinearity arises primarily due to weak Dzyaloshinskii–Moriya interactions[69,70] and spin frustration effects, which become significant below the Néel temperature (~ 40 K), as supported by neutron diffraction and magnetic susceptibility data.[60] However, bulk Co_3O_4 is generally characterized by a collinear antiferromagnetic arrangement of high-spin $Co(II)$ centers, with a weak antiferromagnetic exchange coupling constant ($J \sim 2$–5 cm^{-1} (ref. 58 and 59)). This weak coupling aligns with the structural composition of Co_3O_4 or $Al_2Co(II)O_4$, where low-spin $[Co/Al(III)O_6]^{9-}$ units in tetrahedral sites act as non-magnetic spacers between the tetrahedral $[Co(II)O_4]^{6-}$ magnetic sites, effectively limiting the strength of magnetic exchange between $Co(II)$ pairs. While in principle such effects might become pronounced in the presence of spin compensated systems,[68,71] the electronic excitations contributing to the optical band gaps predominantly stem from the local ligand field and charge transfer transitions at individual or pairwise interacting Co sites which are well described within the

framework of this collinear antiferromagnetic arrangement. In fact, these localized excited states exhibit only weak sensitivity to spin canting or non-collinear effects that influence long-range magnetic order. Consequently, it is not expected that such phenomena would alter the nature of the involved excited states. Given this, investigating non-collinear magnetism interactions in bulk Co_3O_4 and its derivatives falls beyond the scope of the present study.

In addition to the experimental studies,[26,29,31–50] several computational investigations[29,72–84] have been performed over the last few decades. Most recent studies combine DFT methods employing GGA-level functionals with periodic boundary conditions.[72–79,81] While this protocol is considered a successful standard for calculating many properties of solid-state systems, it is also known that pure DFT functionals, in particular, tend to underestimate band gaps, mainly due to the self-interaction error.[85–88] An improvement can be expected by using hybrid functionals or determining the band gap utilizing Green's function methods,[88,89] as has been done for Co_3O_4.[75–77,79,81,82] However, in our opinion, post-Hartree–Fock methods are more promising candidates for accurate calculations of optical excitations, and we provide computational evidence for this claim in the present work.[90,91]

Recent studies have demonstrated the potential of using electrostatic embedding approaches to model solid-state systems.[90,92–104] The advantage of using embedded cluster models is that all established methods in molecular quantum chemistry are immediately applicable, which is not the case for methods that insist on periodic boundary conditions. In a number of cases, it has been demonstrated that cluster calculations performed with sufficiently large quantum regions converge to the results of periodic calculations provided the same density functionals are used.[90,95–101] In particular, studies on the calculation of optical band gaps with linear response methods on various embedded cluster sizes have shown that accurate band gap results can be successfully obtained with equation of motion coupled cluster (EOM-CC) methods and results comparable to periodic calculations with time-dependent DFT (TD-DFT).[90,94]

Another hurdle in the computational description of Co_3O_4 is that it is argued to be a highly correlated material despite the weak antiferromagnetic coupling between the $Co(II)$ centers. This arises from strong electron interactions, mixed valency effects, and competing superexchange pathways, among other factors.[29,75,105,106] Single-reference methods such as DFT are restricted in their capacity to describe such phenomena.[107–109] One solution to this shortcoming is to treat these materials with a DFT+U approach in periodic boundary calculations.[110] This approach has been applied to Co_3O_4 in multiple studies.[72–75,77–79,81,83,84] The procedure is reported to distort the materials' electronic structure,[75] which might lead to correct band gap magnitudes but limits the prospect of an accurate analysis of its character. For transition metal complexes and other molecular systems, post-Hartree Fock methods such as state averaged complete active space self-consistent field (SA-CASSCF)[111–113] can handle highly correlated materials

17226 | *Phys. Chem. Chem. Phys.*, 2025, **27**, 17225–17244

This journal is © the Owner Societies 2025

by itself or in combination with perturbation methods such as NEVPT2.[114–116] In fact recent advances of approximate configuration interaction (CI) wavefunction based methods on the basis of the density matrix renormalization group (DMRG),[117] the iterative configuration expansion (ICE-CI)[118,119] or the full configuration interaction quantum monte Carlo (FCIQMC)[120] in treating large active spaces have been proven instrumental for the computation of the magnetic anisotropy or the low lying valence excitation spectrum of multimetallic centers.[121–124]

In this paper, we investigate the band gap problem of Co_3O_4. For this purpose, it is necessary to introduce to our analysis in addition to Co_3O_4, the auxiliary systems $Co(III)_2ZnO_4$ and $Al_2Co(II)O_4$. These systems are specifically chosen to serve as isolated representations of either the $Co(III)$ or $Co(II)$ sites. In this study, the approach to the band gap problem combining the electrostatic embedding protocol with TD-DFT and EOM-CC[90] will be picked up and extended to open-shell systems by employing a systematic series of post-Hartree Fock multireference methods that are based on CASSCF or CASCI wavefunctions in combination with, among others, NEVPT2[114–116] and CASPT2,[125,126] as well as MR-EOM-CC,[127] and ICE-CI.[118,119] The current study aims to provide insight regarding the number and the origin of band gaps in Co_3O_4, as well as the role of the local CoIII/CoII sites to this fundamental property.

II. Definition of the band gaps

Entering the discussion, it is instrumental to first comment on the nature of the band gap (BG) and its relationship to excitation energies in an effort to bridge between the nomenclature used in solid state physics and molecular quantum chemistry. In a nutshell, different types of band gaps reveal different aspects of a material's electronic and optical properties.[30]

As illustrated in Scheme 1 for an N electron 'neutral' system the fundamental (or transport) band gap, defined by the difference between ionization potential (IP^N) and electron affinity (EA^N), determines the energy needed to generate free charge carriers.[128]

The optical band gap is the lowest energy required for an optically allowed (dipole-allowed) excitation from the ground state $|\Psi_0^N\rangle$ to an excited state $|\Psi_1^N\rangle$ that possesses sufficient oscillator strength to contribute observably to the absorption spectrum. This transition defines the absorption onset of the material. In this process, the electron and hole remain bound as an exciton. The exciton binding energy (E_B) is the difference between the transport and optical gaps.[129] This quantity is significant in molecules and molecular crystals, but often negligible in inorganic solids.[30]

The excitation defining the optical band gap typically occurs to a state of the same spin multiplicity as the ground state (e.g., singlet–singlet or triplet–triplet), following spin selection rules. Not all low-energy excitations are optically active: dipole-forbidden transitions can occur where selection rules suppress optical intensity, resulting in very weak or absent absorption features despite energetically allowed transitions.[129]
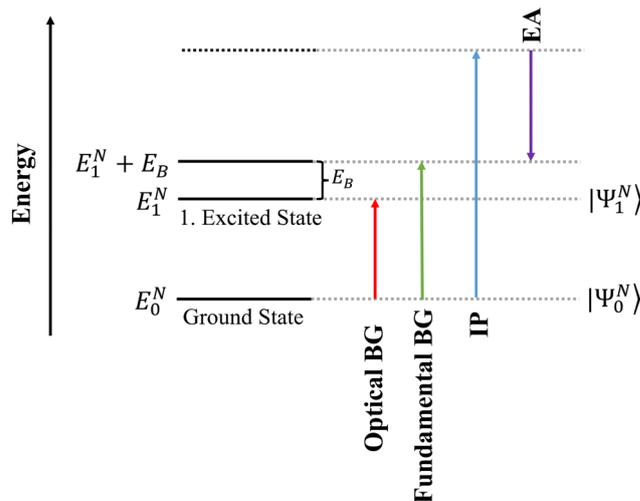
Scheme 1 Schematic representation of optical *versus* fundamental (or transport) band gaps in a chemical system.

In addition to optical selection rules, the momentum relationship between electronic states also shapes absorption behavior. Optical transitions in direct band gap materials are strong and vertical, while indirect gaps lead to weaker absorption onsets due to the need for phonon involvement. The distinction between direct and indirect band structures applies to both fundamental and optical band gaps but is most apparent in optical absorption measurements. This work focuses on direct optical band gaps.

The optical band gap can be experimentally determined using UV/Vis spectroscopy, for instance through Tauc plot analysis.[130] Unlike the optical gap, the fundamental band gap is not limited to dipole-allowed transitions and does not necessarily show up in UV/Vis spectra. Experimentally it can be accessed through techniques like photoemission and inverse photoemission spectroscopy that probe the energies of occupied and unoccupied states separately.

While band gaps indicate energy thresholds with the optical band gap indicating the minimum energy required for the electronic excitation, excited states fully describe the electronic configuration after excitation, including changes in spin, orbital character, and symmetry. In optical spectra, absorption bands arise from ensembles of such excited states, but only those that are dipole-allowed and have significant oscillator strength contribute observable intensity. The optical band gap is thus associated with the onset of absorption, defined by the lowest-energy optically active (dipole-allowed) excited state.

As has been discussed in detail,[90] various approaches may be used to compute optical and fundamental band gaps ranging from particle/hole to wavefunction based methodologies that impact both the predictive accuracy as well as the nature of the computed band gaps. Regardless of the method utilized, in this work the optical band gap is defined computationally as the energy of the first excited state with appreciable oscillator strength.

This journal is © the Owner Societies 2025

Phys. Chem. Chem. Phys., 2025, **27**, 17225–17244 | **17227**

III. Literature overview

Over the last few decades, many measurements of the absorption spectra of Co_3O_4 and the related optical band gaps have been published. Fig. 1a shows a selection of experimental absorption bands[29,32–38,51–57,131–134] of Co_3O_4, while Fig. 1b illustrates the experimental (optical) band gaps.[26,29,31–50] In the ESI,† Table S1 documents details of the experimental results, measurement techniques, materials, and more. This section outlines the main results with the aim of providing reference values for subsequent band gap calculations and to give a first insight into their possible origins.

(a) Number of band gaps in bulk Co_3O_4

A number of two to five absorption bands have been experimentally observed depending on the employed wavelength range. One or two overlapping absorption bands at 0.82 eV ± 0.03 eV and 0.94 eV ± 0.01 eV were identified in the absorption spectra, including NIR in addition to UV/Vis. A lower energy band at 0.56 eV was also mentioned in some references, ref. 42 and 135. The most prominent bands were identified at 1.70 eV ± 0.07 eV and 2.93 eV ± 0.28 eV. The intensity increased and the peaks broadened with increasing energy.

Most references, ref. 32–39 and 42–50, agree that Co_3O_4 has two optical band gaps related to the latter two absorption bands with average values of 1.70 eV (ranging from 1.50 eV[51] to 1.95 eV[56]) and 2.93 eV (ranging from 2.20 eV[29] to 3.55 eV[56]). Although the first dipole-allowed transition state is usually the optical band gap, there is some disagreement as to whether the first band in the absorption spectrum at about 0.82 eV should be associated with a band gap. Some references have not assigned a band gap to this energy range although identifying the absorption bands.[33,37,38,135] In contrast, others have identified a band gap[29,34] with an average value of 0.75 eV ± 0.04 eV or 0.78 eV ± 0.05 eV, including Waegle et al.,[37] naming it a 'midgap' instead of a band gap.

In summary, Co_3O_4 is typically reported to exhibit two prominent optical band gaps associated with absorption bands near 1.70 eV and 2.93 eV, while the lower-energy bands remain the subject of ongoing debate.

(b) Selection of reference experimental data sets

Based on the above experimental observations, it is essential to understand the differences in the band gap values obtained to determine the best reference values for subsequent band gap calculations. The band gap energy of the material seems to be primarily influenced by crystallization and finite-size effects, and its origin is mainly attributed to the experimental preparation method of the material. Most studies have used thin films for measurement,[26,29,31–35,37–43,45–50,52,54–57,133,136] although some have used ceramic[51,53,134] or powder samples.[135]

Focusing on thin film samples, various preparation methods have been reported including sintering,[55,134] spray pyrolysis,[56,57] sol–gel methods,[55,133,135] physical vapor deposition (PVD),[34,37,38,52,54,56] or chemical vapor deposition (CVD).[32,33,35] The results seem to be more consistent for thin films, especially those prepared by PVD. However, film thickness also affects absorption bands and band gaps, with PVD films typically being thinner and resulting in higher band gap energies. Nkeng et al.[56] suggests that measurements on films thinner than 0.1 μm may be less accurate. The substrate of the thin film also influences the optical properties, with higher roughness on glass leading to higher peak positions of the absorption band compared to silica.[57] More information on the relationship between material preparation and band gap can be found in the ESI,† Fig. S1.

Based on these observations, the data included in the band gap determination are only measurements from thin films with a thickness of at least 0.1 μm, excluding those prepared by spray pyrolysis as they were least consistent, and with maximum error values significantly different from the mean absolute error (MAE). Hence, the first absorption band ranges for the selected data from 1.65 eV to 1.70 eV with a mean of
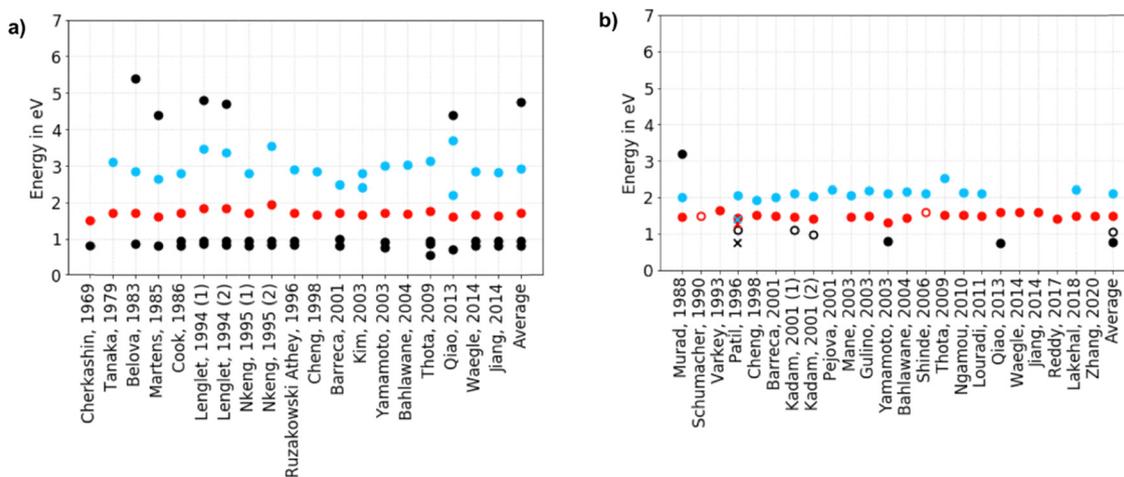
Fig. 1 Overview of experimental (a) absorption bands[29,32–38,51–57,131–134] and (b) band gaps[26,29,31–50] found in the literature. Red and blue symbols: the two most frequently reported band gap values – approx. 1.51 eV (red) and 2.14 eV (blue) – along with their associated absorption features. Black symbols: other reported absorption bands and band gaps. Filled circles: direct band gaps. Empty circles: indirect band gaps. Cross: forbidden gaps.

17228 | *Phys. Chem. Chem. Phys.*, 2025, **27**, 17225–17244

This journal is © the Owner Societies 2025

1.67 eV $\pm$ 0.02 eV and a median of 1.65 eV. The corresponding band gap ranges from 1.50 eV to 1.52 eV with a mean of 1.51 (1.505) eV $\pm$ 0.01 (0.007) eV and a median of 1.50 eV. The next higher absorption band ranges from 2.75 eV to 2.85 eV with a mean of 2.81 eV $\pm$ 0.04 eV and a median of 2.83 eV. The corresponding band gap ranges from 2.00 eV to 2.20 eV with a mean of 2.14 (2.135) eV $\pm$ 0.07 (0.068) eV and a median of 2.17 eV.

In the absence of a larger data set for the lowest band gap with a mean of 0.78 eV $\pm$ 0.05 eV, this value is accepted for this band gap. This seems justified as the available data indicate that this band gap does not seem to be as affected by material preparation factors.

(c) The character of the experimentally observed band gaps

The band gaps shown in Fig. 1b are predominantly optical in nature and are derived from Tauc plot analysis of transmission data. Depending on the excitation process, optical band gaps can be classified as direct or indirect.[137] The three band gaps reported above at 0.78 eV, 1.51 eV, and 2.14 eV are commonly reported as direct, but two studies have identified the band gap at 1.51 eV as indirect.[40,47] Patil et al.[42] and Kadam et al.[43] reported an indirect band gap with a mean value of 1.06 eV $\pm$ 0.05 eV and found additional direct and indirect band gaps. These band gaps are irrelevant to the present discussion since only direct optical band gaps are considered. Qiao et al.[29] reported a band gap of 0.76 eV as fundamental rather than optical.

The question arises regarding the origin of the various direct optical band gaps in Co_3O_4. Many of the experimental studies[33,39,42,43,47,50,135] explain the band gaps located at 1.51 eV and 2.14 eV in terms of the band structure based on the 1987 computational work of Miedzinska et al.[138] In these explanations, the conduction band is usually dominated by Co(II) t_2 (3d) orbitals and the valence band is dominated by O 2p orbitals. The resulting interband transition gives rise to the so called 'true'[33] band gap at 2.14 eV, identified as LMCT O 2p $\rightarrow$ Co(II) $3e_g$. The presence of Co(III) (3d orbitals) leads to a 'sub-band'[33] in the energy gap, resulting in the optical band gap at 1.51 eV, often identified as MMCT Co(III) t_{2g} $\rightarrow$ Co(II) t_2[32,34,35] or Co(II) t_2 $\rightarrow$ Co(III) e_g,[135] or as LMCT O 2p $\rightarrow$ Co(III) e_g.[33,48,50]

The band gap picture presented by Miedzinska et al.[138] can be supported by the results of experimental investigations to characterize the band gap. For example Martens et al.[53] observed increased absorption features at 0.8 eV, 1.6 eV, and 2.6 eV when they replaced the octahedral Fe sites in $CoFe_2O_4$

with Co(III), changing the system to Co_3O_4. They concluded that the octahedral Co(III) sites caused the absorption features. However, the result also opens the possible interpretation that the tetrahedral Co(II) sites or both could also contribute. Schumacher et al.[40] identified the 1.50 eV band gap as resulting from the ligand field transition of the octahedral Co(III) site based on Martens et al.[53] observation. Kim et al.[133] studied the substitution of tetrahedral Co(II) sites by Zn in Co_3O_4 to form Co_2ZnO_4. They found a gradual decrease in the absorption bands at 1.65 eV and 2.4 eV, indicating the importance of the Co(II) sites for these features. They also observed that the higher and broader band associated with the 2.14 eV band gap in Co_3O_4 contains two peaks at 2.4 eV and 2.8 eV. Substitution of Co(II) sites with Zn shifted this feature to the higher peak, suggesting that this absorption band may be an overlap of at least two different transitions, with its upper part potentially related to Co(III) sites and its lower part related to Co(II) sites. Jiang et al.[38] related the band at 2.81 eV to Co(III) based on oxidation state-sensitive measurements with XUV and claimed it to be LMCT based on Miedzinska et al.[138] The previously reported experimental results are summarized in Table 1.

(d) Summary of published computational studies

In the discussion so far, a collection of experimental methods supports the existence of three band gaps reported for the bulk Co_3O_4 located at 0.78 eV, 1.51 eV, and 2.14 eV. Several theoretical studies have addressed the band gap problem in bulk Co_3O_4, often with the main goal of accurately reproducing one or more of the band gaps and also relating them to the band structure of the material. A detailed literature overview of multiple existing computational studies[29,52,72–84,138,139] is provided in the ESI,† in Section S2 (ESI). The following passage highlights the most important aspects.

As highlighted above, despite extensive experimental studies, the primary source of information is still based solely on the theoretical study of Miedzinska et al.[138] who modeled the system without periodic boundary conditions – modeling a unit cell using a semiempirical method. However, the majority of the reported computational studies, especially the more recent ones, on the Co_3O_4 band gap problem are based on periodic boundary conditions applying DFT.[29,61,72–84]

Most commonly, the pure GGA functional has been used with an emphasis on PBE.[29,61,72–84] However, there are examples of studies using LDA,[76] hybrid functionals,[75,76,79,81] and Green's function methods.[75,77] The Green's function methods yielded band gaps in good agreement with the first band gap of

Table 1 Experimental evidence (using UV/Vis measurements unless stated otherwise) supporting site-specific assignments of absorption features and their related band gaps in Co_3O_4

Study	Observation/experimental method	Absorption features influenced	Proposed site contributions/interpretation
Martens et al.[53]	Substitution of Fe with Co(III) in $CoFe_2O_4$ $\rightarrow$ Co_3O_4	0.8, 1.6, 2.6	Mainly octahedral Co(III), possibly also Co(II)
Kim et al.[133]	Zn substitution for tetrahedral Co(II) $\rightarrow$ Co_2ZnO_4	1.65, 2.4; later split into 2.4, 2.8	Tetrahedral Co(II) (1.65, lower part of 2.4); Co(III) (2.8, upper part of 2.4), split; suggests overlap of transitions
Jiang et al.[38]	XUV spectroscopy with oxidation-state sensitivity	2.81	Octahedral Co(III), assigned as LMCT

This journal is © the Owner Societies 2025

Phys. Chem. Chem. Phys., 2025, **27**, 17225–17244 | **17229**

0.78 eV. Notably, LDA and the pure GGA functional tended to underestimate the band gaps, as known for these types of functionals,[140] often approaching zero.[72,74–77] Given the highly correlated nature of Co_3O_4, the GGA+U approach, which incorporates an effective on-site potential, commonly used for such materials,[75] is employed in many of these studies[63,72,75,81,83,84] to align the calculated band gap energies with experimental values. While this method is efficient in obtaining the desired band gap value, it can also lead to undesirable changes in the electronic structure of the system.[75]

Computational studies[29,80] analyzing the band gap character focusing on GGA functionals agree with Miedzinska et al.[138] that the band gaps at 1.51 eV and 2.14 eV are dominated by MMCT and LMCT transitions. The studies[29,52,139] that include the excitation at 0.78 eV state that this could be due to Co(ɪɪ) ligand field transitions. However, Lima et al.[82] proposed in their study calculating the band gaps with hybrid functionals that Co(ɪɪ) and Co(ɪɪɪ) ligand field transitions are the origin of the 1.51 eV and 2.14 eV band gaps, arguing that the MMCT and LMCT transitions are unlikely to occur at energies as low as the band gap values.

Uncertainties remain due to the exclusion of the multireference character in the calculation methods.

IV. Computational details

The calculations were performed using the Orca 5.0.1 and 6.0.1 suite of programs.[141–145] The present calculation protocol consists of a number of steps outlined below.

The first step involves the calculation of excited states using TD-DFT applied to multimetallic clusters of increasing size representing the cobalt oxides Al_2CoO_4, Co_2ZnO_4, and Co_3O_4 in the framework of the electrostatic embedding approach treated with ionic-crystal-QM/MM as described in more detail below. Since the goal is to study the band gaps of Co_3O_4, the atomic positions used for the Al_2CoO_4 and Co_2ZnO_4 models are equivalent to Co_3O_4. The functional PBE0[146,147] is used. Depending on the system, the calculations include spin–orbit coupling (SOC) effects, spin flip, and/or broken symmetry. In all calculations, scalar relativistic corrections are applied using the second-order Douglas Kroll Hess (DKH2)[148,149] scheme.

In the converged models, the excited states are computed at the CIS, EOM-CCSD level of theory (referred to as EOM-CC),[150–152] and multiple TD-DFT methods, including a variety of DFT functionals, namely (meta-)GGA functionals (BP86,[140,153] PBE,[154] TPSS,[155] B97-3c,[156] BLYP,[153,157] r^2Scan-3c[158]), hybrid functionals (PBE0,[159,160] B3LYP,[153,157,160] B1LYP,[153,157,160] TPSSH[155,159,161]) as well as double-hybrid functionals (DSD-PBEP86,[162] ωPBEPP86,[163] SCS-ωPBEPP86,[163] B2PLYP,[164] ωB2PLYP,[165] DSD-BLYP[166,167]). To speed up the EOM-CC calculations, selected atoms in the cluster were included at the Hartree–Fock level within the ionic-crystal QM/MM scheme. Comparison calculations showed that the inclusion of this approximation does not change the excitation energy of the excitations studied in the respective context.

The next step revises the excited states by developing a protocol beyond the single-reference methods based on a series of multireference post-Hartree Fock methods. Localized molecular orbitals were employed to define the active spaces in all multireference calculations, ensuring a chemically meaningful and stable description of the electronic structure. The various employed methods of increasing accuracy are CASSCF,[111–113] CASSCF/DCD-CAS(2),[168] CASSCF/CASPT2,[125,126] and CASSCF/NEVPT2,[114–116] as well as MR-EOM-CCSD[127] (referred to as MR-EOM-CC). Results obtained from CASSCF/DCD-CAS(2) and CASSCF/CASPT2 calculations are provided in the ESI,† as they closely match the trends obtained at the CASSCF/NEVPT2 level and do not alter the main discussion. Furthermore, ICE-CI and CAS-ICE[118,119] and a development version of our recent CAS-ICE/NEVPT2 variant were employed utilizing various active spaces in the sequence (CAS(14,10)), (CAS(20,15)) and (CAS(26,20)), to involve all necessary interactions arising from the formal Co(ɪɪ) and Co(ɪɪɪ) centers.

Prior to the excited states investigation in a similar fashion the ground state magnetic structure of the antiferromagnetically coupled Co(ɪɪ) centers in Co_3O_4 is computed employing BS-DFT, CAS-ICE and CAS-ICE/NEVPT2 levels of theory in various active spaces (CAS(14,10) and CAS(20,15)).

A series of DKH-def2-XVP[169,170] and cc-pVXZ-DK[171] basis sets were tested for all methods. For the DFT calculations, the performance of DKH-def2-XVP appeared satisfactory, and the sequence of DKH-def2-SVP, DKH-def2-TZVP, and DKH-def2-QZVPP basis sets indicated that DKH-def2-TZVP was sufficient. These were used for the TD-DFT convergence scheme, as mentioned above, while DKH-def2-QZVPP was used for the final TD-DFT results. The DKH-def2-XVP basis sets were used together with the auxiliary basis sets def2-XVP/C and def2/J.

For the post-Hartree Fock methods, cc-pVXZ-DK outperformed DKH-def2-XVP in terms of convergence in the respective sequences. In the post-Hartree Fock calculations, cc-pVQZ-DK and its auxiliary basis sets[172] are used if not noted otherwise. Table S4 in the ESI,† shows the results for the different methods and basis sets, which will not be discussed further in this paper. Examples of input files are also given in the ESI,† in Section S6.

Within the electric dipole approximation (EDA) the excited states reached by the ground state are categorized as dark or non-dark states according to the magnitude of the calculated oscillator strengths of the respective EDA transitions. This implies that a non-dark state is reached by EDA transitions with oscillation strengths that are larger than 0.001 a.u. Likewise, dark or electric dipole-forbidden states are reached by EDA transitions with oscillation strengths that are lower than 0.0001 a.u. Intermediate cases of 'partially' allowed EDA transitions will then lead to 'partially' or 'potentially' non-dark states. The inclusion of the latter distinction avoids the false exclusion of states that are non-dark in the experiment, but have low intensity in the employed computational model due to deficiencies of the oscillator strengths computation.

17230 | Phys. Chem. Chem. Phys., 2025, 27, 17225–17244

This journal is © the Owner Societies 2025

V. The electrostatic embedding model of the crystal structures

Co_3O_4 crystallizes in the space group $Fd\bar{3}m$. It is a spinel mixed-valence compound with two different Co sites, the tetrahedral (T_d) site with a local high spin Co(II) center and the distorted octahedral (D_{3d}) with a local low spin Co(III) center. The Co(II) sites are antiferromagnetically coupled, resulting overall in an open singlet in the ground state. The Co–O bond lengths are 1.955 Å for Co(III) and 2.025 Å for Co(II). Al_2CoO_4 and Co_2ZnO_4 are derivatives of Co_3O_4. In Al_2CoO_4, the octahedral Co(III) sites are replaced by Al(III), resulting in an antiferromagnetic solid. In Co_2ZnO_4, the tetrahedral Co(II) sites are replaced by Zn(II); therefore, the system is diamagnetic. The crystal structures are shown in Fig. 2.

The crystal structures are modeled on the basis of the electrostatic embedding approach. As described before,[90,92] this approach requires dividing the cluster model into three domains: the quantum cluster (QC), the boundary region (BR), consisting of 'capped' effective core potentials (cECPs), and the point charge (PC) region. A representative embedded cluster is provided in Fig. 3a. The QC region is the part of the model where the employed quantum chemical calculation takes place. Therefore, the cluster needs to be representative of the structure of the computed solid. In the case of Co_3O_4, the QCs are combinations of tetrahedral Co(II) and distorted octahedral Co(III) sites in a ratio of 1:2, which preserve the respective coordination environments of the oxygen atoms around the Co centers. Fig. 3b shows the series of QCs where 't' abbreviates the tetrahedral sites and 'o' the distorted octahedral sites. Both sites are also considered in isolation ($[Co(II)O_4]^{6-}$ – '1t' and $[Co(III)O_6]^{9-}$ – '1o'). A corresponding series is also considered for Al_2CoO_4 and Co_2ZnO_4.

VI. Band gap characteristics within the electric dipole approximation

As discussed above, the optical band gap is associated with the lowest-energy dipole-allowed excitation. Therefore, the following focuses on analyzing the character of low-lying optical excitations in Co_3O_4 to identify suitable candidates for the experimentally observed optical band gaps. In a first approximation where spin–orbit coupling and vibronic coupling phenomena are considered to be small, optical band gaps are the first dipole-allowed excited state in a system. Identifying this state requires evaluating which electronic transitions are permitted by dipole selection rules. While this question is often straightforward, this consideration becomes more complex in extended solids such as Co_3O_4, where not only numerous competing excitations and different symmetries may be involved, but the possibility of multiple optical band gaps must also be considered. To deal with this complexity, a first step is to focus on the local excitations and symmetries of the two cobalt sites within the solid.

Fig. 4a and b show the excitation models adopted within the one-electron approach of the two isolated cobalt sites. The isolated octahedral O_h $[Co(III)O_6]^{9-}$ site (1o) is distorted and hence, has (D_{3d}) symmetry obtaining a low spin $3d^6$ electron configuration. The ligand field transitions Co(III) $3d_{xy,xz,yz} \rightarrow 3d_{x^2y^2,z^2}$ ($t_{2g} \rightarrow e_g$); $^1(T_{1g} + T_{2g})$ in the approximated O_h or $e_g \rightarrow e_g/a_{1g}$; $^1(A_{1g} + [A_{2g}] + (E_g))/^1E_g$ in the D_{3d} symmetry are electric dipole-forbidden. Hence, the resulting states are expected to have no or little intensity and thus, will likely result in dark states. This strongly suggests that they are unlikely to contribute to the origin of the optical band gap. However, the dipole selection rules might be altered by (1) intensity borrowing mechanisms,[173–175] (2) higher moment contributions, (3) vibronic coupling or (4) SOC effects. Therefore, formally electric-dipole forbidden transitions cannot be completely excluded from optical band gap considerations. The first electric dipole-allowed excited state in the Co(III) site is of LMCT characteristic consisting of electron excitations O 2p $\rightarrow$ Co(III) $3d_{x^2y^2,z^2}$ (t_{1u}, $[\cdots] \rightarrow e_g$; $^1(T_{1u} + T_{2u})$ in the approximated O_h or e_u, $[\cdots] \rightarrow e_g/a_{1g}$; $^1(A_{1u} + A_{2u} + E_u)/^1E_u$ in the D_{3d} symmetry).

In the isolated tetrahedral site $[Co(II)O_4]^{6-}$ (1t) in the high spin $3d^7$ electron configuration, the Co(II) $3d_{x^2y^2,z^2} \rightarrow 3d_{xy,xz,yz}$ ($e \rightarrow t_2$; $^4(T_1 + T_2)$) transitions are electric dipole-allowed, and therefore, can be taken into account in the band gap discussion below. The LMCT states originating from O 2p $\rightarrow$ Co(III) $3d_{xy,xz,yz}$ (e, $[\cdots] \rightarrow t_2$ $^4(T_1 + T_2)$) transitions are electric dipole-allowed as well but expected at higher energies than the ligand field transitions.
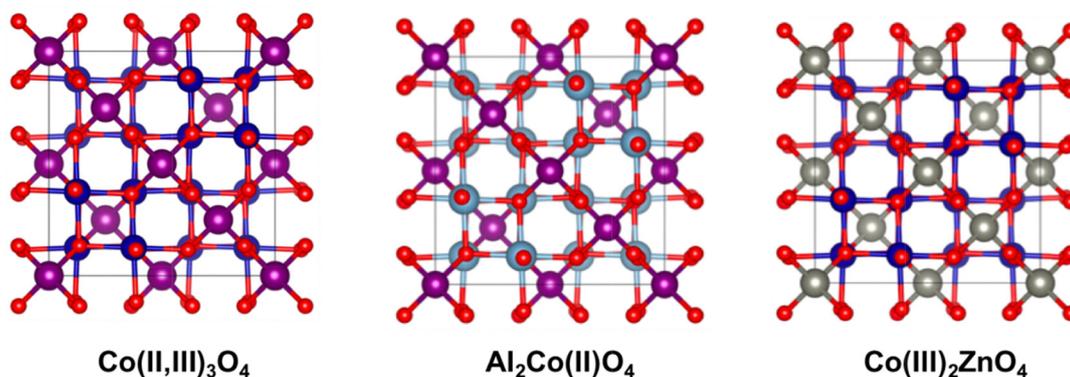
Fig. 2 Crystal structures of the spinel Co_3O_4, $Al_2Co(II)O_4$ and $Co(III)_2ZnO_4$. Color coding: Co(III) (blue), Co(II) (purple), Al(III) (light blue), and Zn(II) (gray).

Co(II,III)₃O₄   **Al₂Co(II)O₄**   **Co(III)₂ZnO₄**

This journal is © the Owner Societies 2025

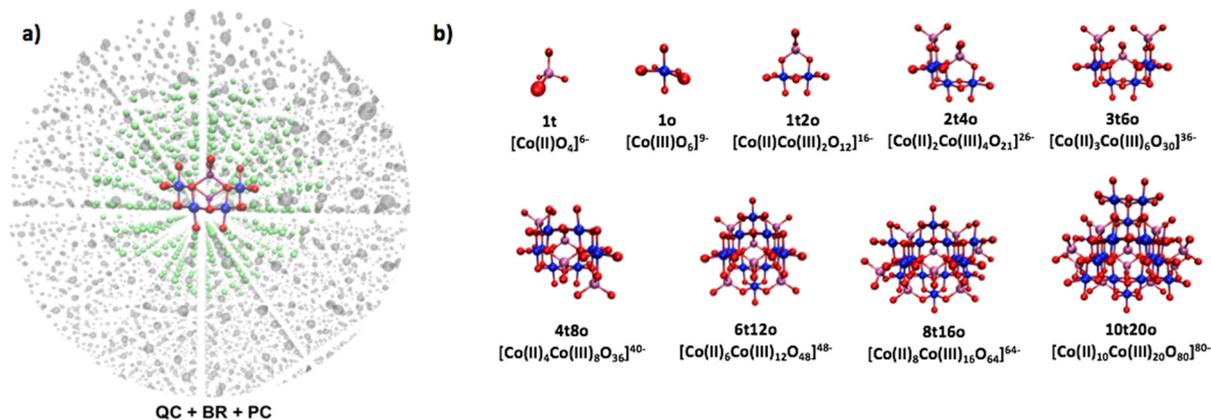*Phys. Chem. Chem. Phys.*, 2025, **27**, 17225–17244 | **17231**

Fig. 3 (a) Graphical representation of the embedded cluster approach for the Co_3O_4 2t4o cluster. Color coding: QC region: Co(II) (purple); Co(III) (blue); O (red). BR/ECPs region: cECPs (green). PC region (grey). (b) Series of Co_3O_4 models for QCs. Nomenclature 't' stands for tetrahedral (T_d – $[Co(II)O_4]^{6-}$) and 'o' for distorted octahedral (D_{3d} – $[Co(III)O_6]^{9-}$) substructures.
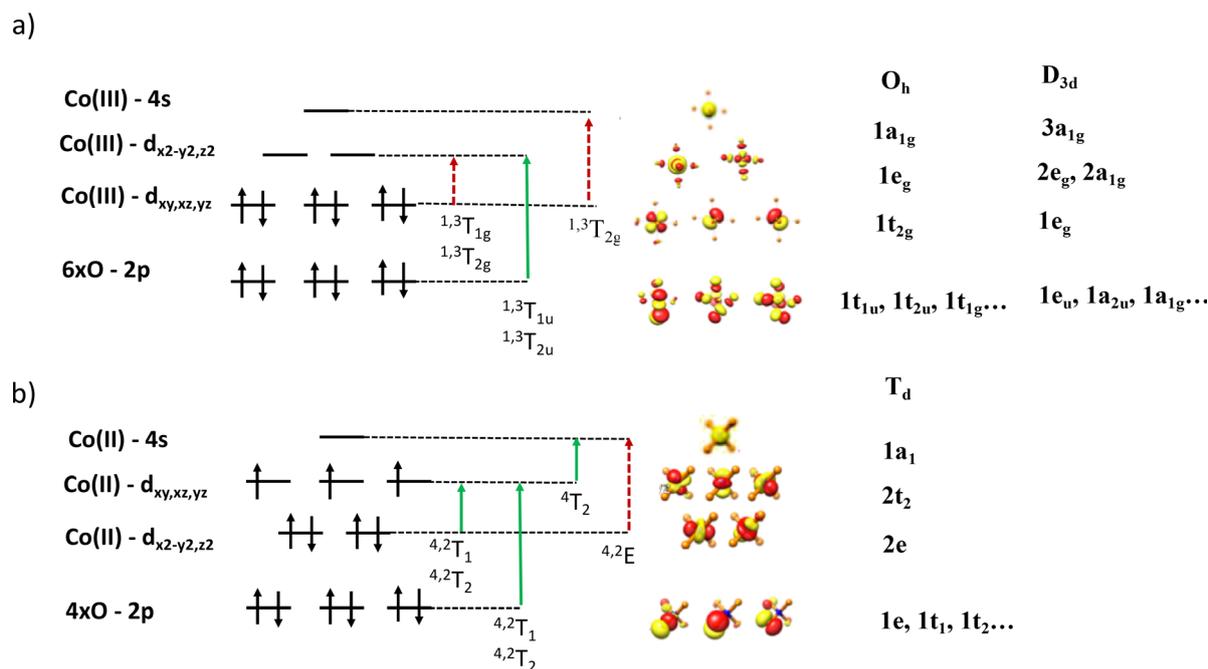

Fig. 4 Schematic representation of excited states in (a) $[Co(III)O_6]^{9-}$ (O_h/D_{3d}) and (b) $[Co(II)O_4]^{6-}$ (T_d). Dotted red lines: electric dipole-forbidden transitions, solid green lines: electric dipole-allowed transitions. Lowercase and uppercase symmetry labels represent orbital and state symmetry labels, respectively.

While the study of isolated cobalt sites provides a first insight into potential excitations for the band gaps, a comprehensive analysis in bulk Co_3O_4 requires the consideration of interactions between these sites. This requires the inclusion of additional MMCT excitations between the different cobalt centers. To accurately represent these interactions, it is essential to construct clusters with sizes beyond a single center as shown in Fig. 3. As the system size increases, the symmetry shifts from the local symmetries to include the centers involved in the specific excitations.

The smallest substructure defining the prospect of an MMCT excitation encloses any two neighboring Co centers. Assuming that the Co(II) and Co(III) centers define M (refer to as A-site) and M′ (refer to as B-site) type of centers, for MMCT

between two Co(II) centers (A–A′), these two Co(II)'s can form C_s or C_{2v} symmetry. Similarly, two neighboring distorted octahedral Co(III) sites, representative of Co(III) → Co(III) M'M'CT (B–B), can have C_s or C_{2v} symmetry. Two nearest centers involved in Co(III) → Co(II) or Co(II) → Co(III) M′MCT/MM'CT (A–B/B–A′) have C_s symmetry. These interactions are shown schematically in Fig. S15 (ESI†). Table 2 summarizes the orbital symmetries of Co–Co pairs in Co_3O_4, based on their pairwise local symmetry (C_s or C_{2v}) within the crystal lattice, and indicates for each MMCT transition type whether it is electric dipole-allowed. Therefore, they could be a potential origin of optical band gaps.

In summary, the first excited states expected in Co_3O_4 are the ligand field transitions local to the tetrahedral and the distorted

17232 | *Phys. Chem. Chem. Phys.*, 2025, **27**, 17225–17244

This journal is © the Owner Societies 2025

Table 2 Orbital symmetries for Co–Co site pairs in Co_3O_4, based on the local symmetry (C_s or C_{2v}) formed by their spatial arrangement within the crystal structure. The Co center pairs considered represent the closest Co(II)–Co(II), Co(III)–Co(III), and Co(II)–Co(III) combinations, reflecting all possible MMCT excitations. The electric dipole-allowed or forbidden nature of transitions are indicated

		C_{2v}	C_s
Orbital symmetry	d_{xy}, d_{xz}, d_{yz}	a_2, b_1, b_2	a', a''
	$d_{x^2-y^2}$, d_{z^2}	a_1	a'
Electric dipole operator symmetry		$A_1 + B_1 + B_2$	$2A' + A''$
MMCT transitions	MMCT/A–A': Co(II) $\rightarrow$ Co(II)	Electric dipole-allowed	Electric dipole-allowed
	M'M'CT/B–B: Co(III) $\rightarrow$ Co(III)	Electric dipole-allowed	Electric dipole-allowed
	MM'CT/A–B: Co(II) $\rightarrow$ Co(III)	—	Electric dipole-allowed
	M'MCT/B–A': Co(III) $\rightarrow$ Co(II)	—	Electric dipole-allowed

octahedral cobalt sites. However, the transition at the octahedral site is dipole-forbidden, making it less likely to contribute significantly to the optical band gap. Consequently, the ligand field transition at the tetrahedral site emerges as the more likely origin of the observed optical absorption onset. Since Co_3O_4 has multiple band gaps, it is also possible that higher excitations such as LMCT and MMCT, which are both dipole-allowed, could be a potential origin. This will be further explored in the following sections.

VII. The nature of the excited states that can be found in the energy range of the band gaps in conventional TD-DFT calculations

Having identified the potential origins of the optical band gaps, the next critical step is to determine which specific excited states occur and exhibit significant intensity within the relevant energy range. To address this, a computational model must accurately capture converged excited states while reflecting the solid-state nature of the system. This is achieved using an electrostatic embedding approach with a range of cluster sizes, from isolated cobalt sites (1o/1t) to the larger 10t20o cluster (see Fig. 3).

The first step involves time-dependent density functional theory (TD-DFT) calculations using the PBE0 hybrid functional, combined with the broken symmetry (BS) approach to account for the antiferromagnetic nature of Co_3O_4. The oscillator strength (f) is used to assess the intensity of each converged excited state, classifying them as:

- Dark states (dipole-forbidden, $f < 10^{-5}$),
- Non-dark states (dipole-allowed, $f > 10^{-5}$) and
- Potentially non-dark states ($f \approx 10^{-5}$).

To gain deeper insight, the analysis extends beyond Co_3O_4 to include its derivative compounds: Al_2CoO_4, representing
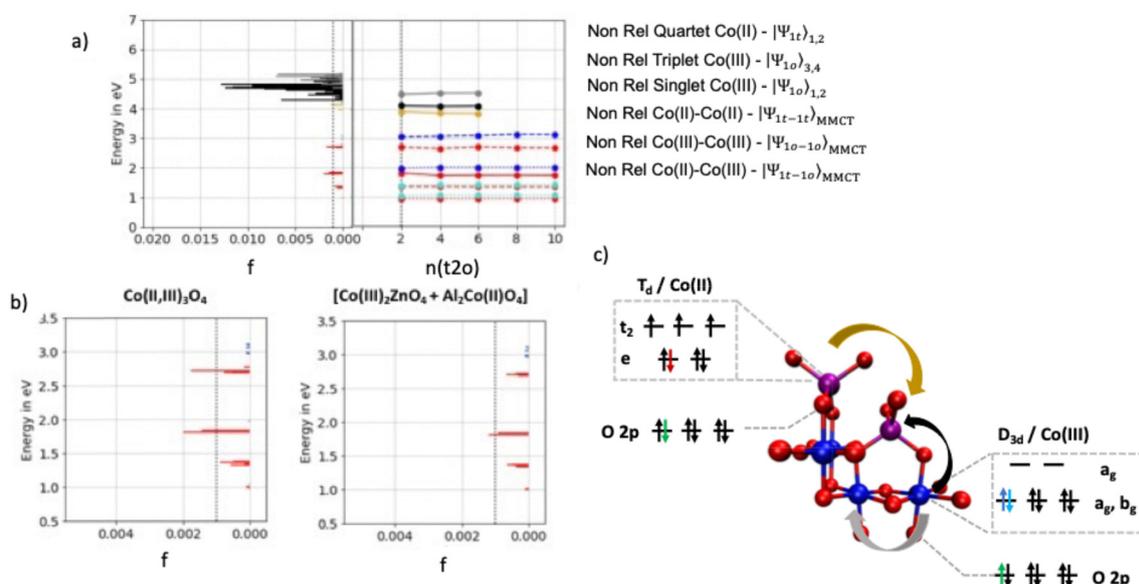
Fig. 5 (a) Broken-symmetry TD-DFT convergence scheme of Co_3O_4 with PBE0/DKH-def2-tzvp. (b) Comparison Co ligand field excitations in Co_3O_4 (left) vs. [Co_2ZnO_4 + Al_2CoO_4] (right) computed with PBE0/DKH-def2-tzvp. Color coding: Co(II) 3d e $\rightarrow$ t_2 excitation (red), Co(III) 3d t_{2g} $\rightarrow$ e_g triplet (turquoise) and singlet excitation (blue), Co(III) $\rightarrow$ Co(III) M'M'CT (gray), Co(II) $\rightarrow$ Co(II) MMCT (yellow), Co(II) $\rightarrow$ Co(III) M'MCT/M'MCT (black); dark states (dotted line), 'potentially' non-dark states (dashed line), and non-dark states (solid line). Oscillator strengths are visualized as horizontal sticks. Dark states are not visible here but are included in the dot representation provided in Fig. S7 of the ESI.†

This journal is © the Owner Societies 2025

Phys. Chem. Chem. Phys., 2025, **27**, 17225–17244 | **17233**

tetrahedral Co(II) sites, and Co_2ZnO_4, representing distorted octahedral Co(III) sites. The excited states for these systems are presented in Fig. S5 and S6 (ESI†) for Co_2ZnO_4 and Al_2CoO_4, and in Fig. 5 for Co_3O_4. These figures display all calculated excited states within the energy range of 0 eV to 6.5 eV for the 2t4o system, highlighting their energy positions and oscillator strengths. This system size is chosen as the low-lying excited states in the band gap region are well-converged for 2t4o clusters. Additionally, the right side of these figures illustrates the convergence of the first or first non-dark excited state of each absorption band across various cluster sizes, ranging from a single cobalt site (1o/1t) up to the largest employed cluster size of 10t20o (see Fig. 3). Dotted, solid, and dashed lines distinguish dipole-forbidden, dipole-allowed, and intermediate states, respectively.

(a) Insights from Co_2ZnO_4 and Al_2CoO_4

Before analyzing the BS TD-DFT results for Co_3O_4, it is valuable to first examine the results for Co_2ZnO_4 and Al_2CoO_4, as they provide insight into the roles of Co(II) and Co(III) centers in the excited-state behavior.

For Co_2ZnO_4, the first set of excited states appears at ~ 1.0 eV and ~ 3.0 eV, corresponding to parent singlet ($|\Psi_{1o}\rangle_{1,2}$) and parent triplet ($|\Psi_{1o}\rangle_{3,4}$) 3d $t_{2g} \to e_g$ ligand field excitations, respectively (see Fig. S11, ESI†). These states are classified as dark, with zero oscillator strength for the first three bands, while the fourth (~ 3.0 eV) exhibits some oscillator strength. Strongly dipole-allowed transitions begin to appear at ~ 4.8 eV, consisting of ligand-to-metal charge transfer (LMCT, O 2p $\to$ Co(III) 3d) and metal-to-metal charge transfer (MMCT, Co(III) 3d $\to$ Co(III) 3d) excitations.

For Al_2CoO_4, BS TD-DFT calculations reveal two main sets of excited states with relevant oscillator strengths in the band gap region. The first set corresponds to ($|\Psi_{1t}\rangle_{1,2}$) ligand field e $\to$ t_2 transitions (see Fig. S11, ESI†), forming overlapping bands between 0.9 eV and 2.7 eV. Some of these bands are exclusive to the BS description, while others appear in both the BS and high-spin (HS) descriptions (see Fig. S6, ESI†), highlighting the influence of the material's magnetic properties on ligand field transitions. The second set, starting at 3.9 eV, corresponds to MMCT Co(II) 3d $\to$ Co(II) 3d excitations, exhibiting significantly higher oscillator strength than the ligand field transitions. LMCT transitions occur at even higher energies and are therefore not relevant for the band gap analysis.

(b) Excited states in Co_3O_4

As shown in Fig. 5, Co_3O_4 exhibits the same set of Co ligand field transitions observed in Co_2ZnO_4 and Al_2CoO_4 with identical energy positions and comparable oscillator strengths. Notably, the oscillator strength of Co(II) 3d e $\to$ t_2 excitations appears slightly enhanced, potentially due to methodological factors or an intrinsic enhancement of Co(II) excitations in the presence of Co(III). However, no additional excited states emerge beyond those seen in the individual Co(II) and Co(III)

systems, justifying the description of Co_3O_4's local ligand field transitions as a sum of the contributions from Al_2CoO_4 and Co_2ZnO_4.

Since all Co(III) ligand field transitions are dark, except for a set of transitions at ~ 3.0 eV, any lower non-dark or 'potentially' non-dark states can be attributed exclusively to Co(II) centers. The higher-energy MMCT states form at 3.9 eV (Co(II) 3d $\to$ Co(II) 3d) and 4.6 eV (Co(III) 3d $\to$ Co(III) 3d), consistent with the findings for Al_2CoO_4 and Co_2ZnO_4. Additionally, an MMCT Co(II) 3d $\to$ Co(III) 3d transition overlaps with these states, emerging at ~ 4.1 eV. However, the inverse Co(III) 3d $\to$ Co(II) 3d transition appears outside the computed excited state range and is excluded due to computational limitations. This exclusion is justified as these states exceed the energy range relevant to the optical band gaps.

Similar to the trends observed in Al_2CoO_4 and Co_2ZnO_4, the MMCT states in Co_3O_4 retain significantly higher oscillator strengths than the local ligand field transitions, reinforcing their dominant role in the optical absorption characteristics of the material.

In summary, the (BS) TD-DFT results indicate that the band gaps primarily originate from ligand field transitions, which dominate the energy range from 0.78 eV to 2.14 eV. The analysis suggests that tetrahedral cobalt sites are the main contributors, as they exhibit significant oscillator strength, whereas the distorted octahedral sites do not. These findings imply that the higher-energy LMCT and MMCT excitations play a negligible role, justifying a focus on ligand field transitions in subsequent investigations. However, given that TD-DFT is known to underestimate band gap energies,[90] and that treating isolated centers may oversimplify the actual system, we aim to refine our approach by employing a more realistic computational model in the following analysis.

VIII. The impact of electron correlation to the band gap energies of Co_3O_4

(a) The nature of the ground and excited states

To better describe the complex excitation behavior in Co_3O_4, we consider multimetallic interactions between the different cobalt sites (A and B). Since the antiferromagnetic coupling between the tetrahedral Co(II) centers (site A) is weak, with a coupling constant J of approximately 2–5 cm^{-1}, the interactions lie well below the Néel temperature (~ 40 K).[58] Within this framework, the ground state $|\Psi_N\rangle$ can be described as a 'neutral' open-shell singlet: each Co(II) center remains locally high-spin (3d^7), but the unpaired electrons on adjacent sites couple antiferromagnetically (i.e., with antiparallel spins), but no formal change in oxidation state occurs (Co(II)–Co(II) pairs). Symbolically, this configuration can be represented as

$$|\Psi_N\rangle \equiv \left| 22 \cdots \overbrace{111}^{Co(II)} \overbrace{-1-1-1}^{Co(II)} 00 \cdots \right\rangle,$$ where the electron populations and spin alignments are shown for the Co(II) sites. Optical excitations from this ground state can involve

17234 | *Phys. Chem. Chem. Phys.*, 2025, **27**, 17225–17244

This journal is © the Owner Societies 2025

on-site ligand field transitions at either the A or B cobalt centers (*e.g.*, d–d excitations), or, if bridging oxygen ligands are involved, ligand-to-metal charge transfer (LMCT) processes. Inter-site transitions between antiferromagnetic Co(II) centers (A–A′) or between Co(II) and diamagnetic Co(III) centers (A–B, B–A′) can give rise to 'ionic' excited states, in which the formal oxidation states at the involved cobalt sites change (*e.g.*, Co(II) → Co(I) or Co(II) → Co(III)). Here, only part of the original antiferromagnetic electron coupling is preserved. In the conventional description, such antiferromagnetic ionic states are accessed from the antiferromagnetic neutral ground state *via* metal-to-metal (MMCT) or metal-to-ligand (MLCT) charge transfer excitations. The strong mixing between neutral, ionic, and charge transfer states in both the ground and excited manifolds leads to a multistate problem, where all relevant configurations must be treated on equal footing. Within this framework, conventional particle–hole theories become insufficient. It is widely recognized that problems of this complexity are best treated with multireference *ab initio* wavefunction methods.[174,176–179]

(b) The role of isolated 'neutral' and 'ionic' states

Based on TD-DFT results indicating that ligand field transitions at the antiferromagnetically coupled tetrahedral Co(II) sites (site A) dominate the optical band gap region, we now investigate these excitations more systematically. Since broken-symmetry TD-DFT does not fully distinguish between 'neutral' and 'ionic' antiferromagnetic ground states, we perform SA-CASSCF calculations from both hypothetical configurations. This approach allows us to systematically distinguish on-site and inter-site contributions at the individual cobalt centers and subsequently investigate how local ligand field excitations evolve in these different electronic environments.

For these calculations, we employ the 2t4o cluster model derived from Al_2CoO_4, focusing on the tetrahedral Co(II) centers. This model provides a representative description of the 'neutral' and 'ionic' configurations of the antiferromagnetically coupled $2S + 1 = 1$ ground state, and captures the relevant on-site and inter-site low-lying optical transitions. Moreover, it exhibits converged excited states within the optical band gap region at the TD-DFT level and satisfactory basis set convergence for the correlated wavefunction methods employed (see Fig. S6 and S12, ESI†). Fig. 6 shows the SA-CASSCF results for this approach, with red denoting ligand field excited states where the system is in the 'neutral' antiferromagnetic ground

$$\text{state} \left| 22 \cdots \overbrace{111}^{Co(II)} \overbrace{-1-1-1}^{Co(II)} 00 \cdots \right\rangle \text{ and purple in one of the}$$

$$\text{'ionic' ones } \left| 22 \cdots \overbrace{110}^{Co(III)} \overbrace{-2-1-1}^{Co(I)} 00 \cdots \right\rangle \text{ which in principle}$$

represents an A–A′ MMCT: Co(II) → Co(II) type of transition. In which locally the Co centers are in Co(I) and Co(III) oxidation states.

When considering only the optically active 'neutral' excited states, the SA-CASSCF results of 2t4o match the excitation
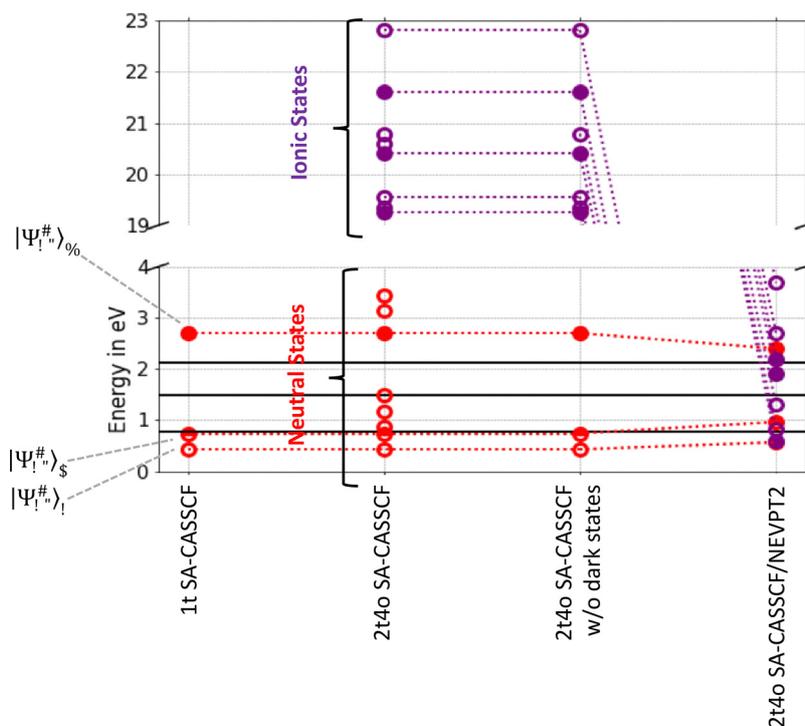
Fig. 6 First excited states of ligand field transitions in Al_2CoO_4 with system size 1t as high spin ($2S + 1 = 4$) and 2t4o computed for 'neutral' (red) and 'ionic' (purple) antiferromagnetic states ($2S + 1 = 1$) with SA-CASSCF and SA-CASSCF/NEVPT2. Dark states (empty circle), 'potentially' non-dark states (half-filled circles), and non-dark states (filled circles).

This journal is © the Owner Societies 2025

Phys. Chem. Chem. Phys., 2025, **27**, 17225–17244 | **17235**

pattern expected for isolated Co(II) centers (1t) and fall within the experimental optical band gap region. In contrast, the 'ionic' excited states lie significantly higher in energy than the 'neutral' ones. However, this situation changes fundamentally upon including dynamic electron correlation through NEVPT2. Despite the simplicity of this model, the results reveal a noteworthy effect: compared to a single high-spin Co(II) site (1t), the band gap energy region contains more excited states with appreciable oscillator strength, arising from inter-site interactions between cobalt centers.

(c)   The role of the isolated cobalt centers

Building on the previous analysis, we now investigate the role of isolated cobalt centers in generating the ligand field transitions observed within the optical band gap region.

In the 2t4o cluster model, dynamic electron correlation (NEVPT2) brings ionic and neutral excited states into energetic overlap without significant interaction. For the 'neutral' configurations, the local ligand field excitations at the tetrahedral Co(II) sites (1t model) reproduce the same pattern and spectral features as the full 2t4o model, while additional excitations associated with the 'neutral' states present in 2t4o correspond to dark states with predominant double excitation character and are thus spectroscopically irrelevant.

To further refine the description of the local ligand field excitations in the 'neutral' configuration, Fig. 7a presents the results obtained for the isolated Co(II) tetrahedral site using higher-level multireference correlation methods. Due to the small active space (five orbitals), advanced treatments such as MR-EOM-CC are computationally feasible and yield excitation energies that closely match both the lower and higher experimental band gap values, aligning well with the SA-CASSCF/NEVPT2 predictions. This analysis confirms that the 1t model provides an accurate description of the bright ligand field excitations at the neutral Co(II) centers. However, both the single-site Co(II) model and the 2t4o model restricted to neutral antiferromagnetic states fail to capture the intermediate experimental band gap feature, highlighting the need to consider additional contributions beyond purely neutral excitations.

Building on the agreement between the single-site (1t) and 2t4o models for the 'neutral' states, we now apply the same approach to the 'ionic' configuration, where the tetrahedral A sites form a coupled Co(I)–Co(III) pair with $3d^8$ and $3d^6$ electron configurations, respectively. Fig. 7b shows that, at the SA-CASSCF/NEVPT2 level, ligand field excitations obtained from isolated tetrahedral Co(I) and Co(III) models (1t) accurately reproduce the optical features of the 2t4o model associated with the 'ionic' antiferromagnetic configuration (Fig. 6). In this comparison, the lowest 'ionic' excited state identified in the
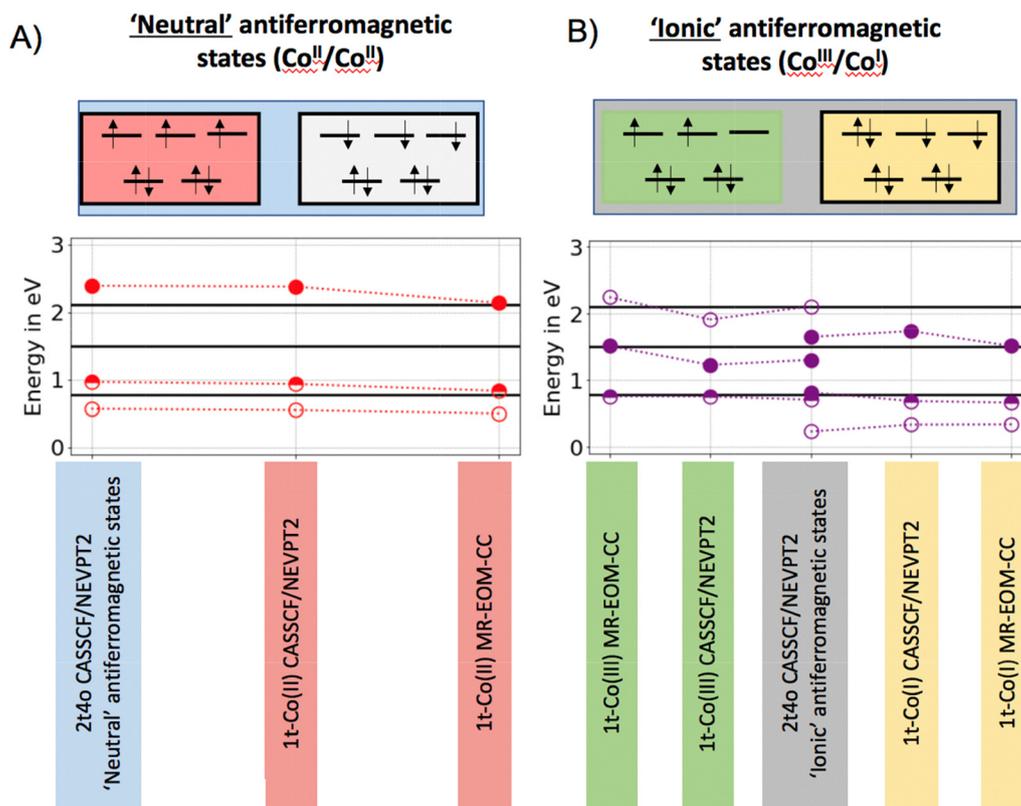
Fig. 7 First excited states of ligand field transitions in the tetrahedral Co sites in Al_2CoO_4 for system size 2t4o with (a) 'neutral' and (b) 'ionic' antiferromagnetic description and 1t with Co centers that are formally Co(I), Co(II) and Co(III) with SA-CASSCF/NEVPT2 and MR-EOM-CC (excitation energies corrected with respect to the 'ionic' antiferromagnetic ground state). Dark states (empty circle), 'potentially' non-dark states (half-filled circles), and non-dark states (filled circles).

17236 | *Phys. Chem. Chem. Phys.*, 2025, **27**, 17225–17244

This journal is © the Owner Societies 2025

2t4o spectrum in Fig. 6 is used as the reference zero (0 eV). The alignment with the isolated models confirms that the optical excitations previously associated with the 'ionic' states in the full 2t4o model can be traced back to local ligand field transitions at tetrahedral Co(I) and Co(III) centers analogous to the 'neutral' case, providing an oxidation-state-specific interpretation of the optical excitations in Co_3O_4.

Applying higher-level MR-EOM-CC calculations to the isolated Co(I) and Co(III) models reveals that both sites contribute optically active excited states that align well with the central experimental band gap around 1.51 eV, which was previously not captured by ligand field excitations of the neutral Co(II) centers. In addition, both sites contribute weak-intensity transitions near the lowest band gap, while the isolated tetrahedral Co(III) site also provides a negligible contribution at the highest band gap, with Co(I) not participating significantly in this region.

The above analysis highlights that MR-EOM-CC ligand field excitations in the tetrahedral Co(I) and Co(III) models fall into the energy region of the central experimental band gap. This suggests that the origin of the central gap may contain significant contributions from local tetrahedral ligand field excitations in the 'ionic' states, arising from on-site transitions at either Co(I) or Co(III) centers. These localized excitations are influenced by site interactions typically associated with A–B (M′MCT) or A–A′ (MMCT) mixing, but the resulting states predominantly retain their ligand field characteristic, rather than representing charge transfer between sites.

However, it should be noted that in TD-DFT analysis (Section VII), explicit A–A′ (MMCT) and A–B/B–A′ (M'MCT) transitions appear only at much higher energies (> 5 eV), well above the energy range of the central band gap (Fig. 5). Moreover, in high-spin TD-DFT calculations (Fig. S6, ESI†), only the lowest and highest experimental optical gaps are reproduced, with no appearance of a central gap. The emergence of the central gap only upon introducing broken-symmetry solutions (Fig. 5) suggests that ionic antiferromagnetic configurations become energetically accessible when spin symmetry is relaxed. Nevertheless, the fact that MMCT transitions occur at high energies indicates that the optical transitions responsible for the central gap are not dominated by inter-site charge transfer but instead arise from on-site ligand field transitions, stabilized and shifted into the gap region by dynamic electron correlation, within a background of ionic electronic structure. Hence it is important to analyze in depth the effect of electron correlation and how it impacts each of the three experimental BGs.

(d) Qualitative treatment of electron correlation and state mixing in BG transitions

In a next step we employ the Hubbard correlation model Hamiltonian[180] and state mixing concepts between ground and excited states in an effort to qualitatively analyze the predominant on-site and inter-site interactions in the three band gap energies and provide a simple numerical justification using the SA-CASSCF/NEVPT2 calculated ingredients of section VIII b.

Hence to better align with the wavefunction-based computations from VIII b we revisit the on-site and inter-site interactions described in the original Hubbard correlation model Hamiltonian by rederiving it in the Born Oppenheimer framework in which one obtains CASSCF and CASSCF/NEVPT2 corrected energies to extract scaling pre-factors to effectively scale down the 'bare' CASSCF integrals that are involved in the chosen set of predominant transitions. While this methodology shares conceptual similarities with TDDFT+U[181] in addressing strong electron correlation interactions, it differs fundamentally by explicitly incorporating multi-reference and dynamic correlation effects rather than relying on an empirical correction parameter. The details of these analyses are provided in Section S5 of the ESI.† Here we briefly discuss the most important points and provide a general summary of the important findings.

In a nutshell starting from the 'neutral' antiferromagnetic ground state configuration state function CSF $|\Psi_N\rangle \equiv |A_p:e^4t_2^3,$ $B:t_{2g}^6, A_q:e^4\bar{t}_2^3\rangle$, we consider in addition the d–d excited state $|\Psi_{ES}\rangle: |A_p:e^3t_2^3, B:t_{2g}^6, A_q:e^4\bar{t}_2^3\rangle$, the LMCT 'ionic' state $|\Psi_{LMCT}\rangle:$ $|O:p^5, A_p:e^4t_2^3, B:t_{2g}^6, A_q:e^4\bar{t}_2^3\rangle$, the A–A′ MMCT 'ionic' state $\left|\Psi_{MMCT}^{A-A'}\right\rangle:\left|A_p:e^4t_2^2, B:t_{2g}^6, A_q:e^4\bar{t}_2^4\right\rangle$, the A–B MM'CT 'ionic' state $\left|\Psi_{MM'CT}^{A-B}\right\rangle:\left|A_p:e^4t_2^2, B:t_{2g}^6e_g^1, A_q:e^4\bar{t}_2^3\right\rangle$, and the B–A′ M′MCT 'ionic' state $\left|\Psi_{M'MCT}^{B-A'}\right\rangle:\left|A_p:e^4t_2^3, B:t_{2g}^5, A_q:e^4\bar{t}_2^1\bar{t}_2^3\right\rangle$, where the bars indicate spin-down electron occupancies and p and q are general orbital indices. These states can mix on the basis of the Hubbard Hamiltonian that in the BO framework reads:

$$H_{Hubbard}^{BO} = \underbrace{h_{pp}^{eff} + J_{pp}^{eff}}_{on\text{-}site} \underbrace{-t_{pq} + J_{pq}^{eff} - K_{pq}^{eff}}_{inter\text{-}site}$$

This relationship implies that there are in principle 5 predominant site interaction terms namely: (1) the on-site crystal field energies h_{pp} (e.g. $\varepsilon_e^{Co(II)}$, $\varepsilon_{t_2}^{Co(II)}$, $\varepsilon_{e_g}^{Co(III)}$, $\varepsilon_{t_{2g}}^{Co(III)}$ or ε_p^O) when an O Ligand is considered, (2) the on-site Coulomb repulsion J_{pp}, (3) the inter-site hopping integral t_{pq} (e.g. t_{AA}, t_{AB}, or t_{AO}, when an O Ligand is considered), (4) the inter-site Coulomb repulsion J_{pq} and (5) the inter-site exchange term K_{pq}.

It should be mentioned that due to the very small antiferromagnetic coupling between the Co(II) A centers (e.g. the two sites are not nearest neighbours, they are separated by Co(III) B-sites) K_{pq} for the A–A′ can be in principle dropped. By setting in addition the reference orbital energy to zero ($h_{pp} = 0$) the above relationship resembles the original Hubbard Hamiltonian.

In a further step we numerically evaluate the relevant terms in order to estimate the energies associated with the ligand field (LF), LMCT and MMCT transitions considered in the model. For this purpose, the values of the 'bare' one and two-electron CASSCF integrals are employed (Tables S5 and S6, ESI†). The effect of electron correlation is considered as a reduction factor to the Coulomb repulsion integrals which is determined by the NEVPT2 stabilization of the 'neutral' and 'ionic' state energies relative to the CASSCF ones (Tables S5 and S6, ESI†). The results are summarized in Table 3.

As seen in Table 3 and further discussed in Section S5 of the ESI,† the ligand field (LF) d–d transition in both the CASSCF

This journal is © the Owner Societies 2025

Phys. Chem. Chem. Phys., 2025, **27**, 17225–17244 | **17237**

Table 3 Numerical evaluation employing a Hubbard like model Hamiltonian to a set of chosen CSFs to represent the predominant d–d, MMCT and LMCT transitions

Character	Energy (eV)	State mixing
Using 'bare' CASSCF 1- and 2-electron integrals		
LF (d–d)	0.77	$3\%|\Psi_N\rangle + 97\%|\Psi_{ES}\rangle$
MMCT	19.5	$33\%\left|\Psi^{A-A'}_{MMCT}\right\rangle + 33\%\left|\Psi^{B-A'}_{M'MCT}\right\rangle + 33\left|\Psi^{A-B}_{MM'CT}\right\rangle$
LMCT	4.44	$10\%|\Psi_{ES}\rangle + 90\%|\Psi_{LMCT}\rangle$
Prescreening the Coulomb integrals from the NEVPT2 energy stabilization		
LF (d–d)	0.79	$5\%|\Psi_N\rangle + 95\%|\Psi_{ES}\rangle$
MMCT	1.91	$20\%|\Psi_{ES}\rangle + 25\%\left|\Psi^{A-A'}_{MMCT}\right\rangle + 30\%\left|\Psi^{B-A'}_{M'MCT}\right\rangle + 30\left|\Psi^{A-B}_{MM'CT}\right\rangle$
LMCT	2.69	$20\%|\Psi_{ES}\rangle + 80\%|\Psi_{LMCT}\rangle$

and NEVPT2 methods, even in this simplified example, falls within the energy region of the first experimental band gap. This is consistent with the value of the tetrahedral ligand field splitting $\Delta\varepsilon_{tetrahedral}$, which mixes only slightly with the 'neutral' ground state $|\Psi_N\rangle$. Similarly, the LMCT transition aligns with the higher-energy experimental band gap transition, though it is slightly overestimated. The numerical example suggests that there is about 10–20% mixing with the d–d transition $|\Psi_{ES}\rangle$.

In agreement with the calculations from section VIIIb, the electron correlation effect appears marginally important, enhancing the mixing with LF excitation. However, the situation changes significantly for the MMCT transition. The numerical example shows that, at the CASSCF level, the states $\left|\Psi^{A-B}_{MM'CT}\right\rangle$ and $\left|\Psi^{A-A'}_{MMCT}\right\rangle$ lie about 18–19 eV. After scaling the Coulomb integrals by about a factor of 9 following the energy stabilization between the CASSCF and NEVPT2 'ionic' states, the transition energies shift into the 1.2 to 3 eV range aligning with the middle band gap energy.

The model predicts a $1:2$ mixing between $\left|\Psi^{A-A'}_{MMCT}\right\rangle \cdot \left|\Psi^{B-A'}_{M'MCT}\right\rangle + \left|\Psi^{A-B}_{MM'CT}\right\rangle$ 'ionic' states along with an additional 20% mixing with the $|\Psi_{ES}\rangle$ transition. This is also consistent with the discussion in section VIIIb, which demonstrated that local Co(I) and Co(III) states exhibit an LF transition that falls within the middle band gap energy range. Notably, these same centers are present in both the $\left|\Psi^{A-A'}_{MMCT}\right\rangle$ and the mixed state $\left|\Psi^{B-A'}_{M'MCT}\right\rangle + \left|\Psi^{A-B}_{MM'CT}\right\rangle$ while the coupling with the A-site $|\Psi_{ES}\rangle$ suggests that the involved sites remain largely isolated.
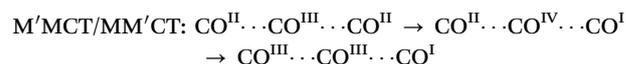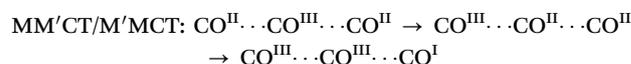
To conclude, although this numerical example remains simplistic, it provides valuable insights into the nature of the three band gap transitions. It particularly emphasizes the dependence of the middle band gap energy on electron correlation among the 'neutral' and 'ionic' states. The state-mixing mechanism goes beyond a simple integral reduction process, necessitating an explicit, simultaneous treatment of all the involved interactions.

(e) Insight into the state mixing mechanism between the cobalt centers

To quantitatively analyze the number and nature of the experimentally observed band gaps in Co_3O_4, we consider the 2t4o model, which consists of two tetrahedral Co(II) centers and four octahedral sites. In the baseline model, the octahedral sites are occupied by Al^{3+} ions to simplify the electronic structure and focus on the contributions of the Co(II) centers. On this model we performed CAS-ICE/NEVPT2 calculations on selected sets of configuration state functions (CSFs) with progressively larger active spaces. The results are shown in Fig. 8. Specifically, CAS(14,10) includes LF, LMCT, and MLCT transitions involving Co(II) tetrahedral centers (2t). In CAS(20,15) and CAS(26,20), one and two Co(III) octahedral centers are explicitly included in the active space, respectively, replacing the corresponding Al^{3+} sites, to capture additional mixing mechanisms involving the Co(III) octahedral centers. Notably, applying a similar approach to the 1t2o model accurately reproduces the magnetic ground state of bulk Co_3O_4, confirming that this methodology provides a balanced description of both ground and excited states. This later analysis is provided in Section S6 of the ESI.†

As shown in Fig. 8A, as soon as states that originate from MM'CT/M'MCT sequences of transitions between the Co^{II} centers and Co^{III} centers:

$$MM'CT/M'MCT: CO^{II}\cdots CO^{III}\cdots CO^{II} \rightarrow CO^{III}\cdots CO^{II}\cdots CO^{II}$$
$$\rightarrow CO^{III}\cdots CO^{III}\cdots CO^{I}$$

$$M'MCT/MM'CT: CO^{II}\cdots CO^{III}\cdots CO^{II} \rightarrow CO^{II}\cdots CO^{IV}\cdots CO^{I}$$
$$\rightarrow CO^{III}\cdots CO^{III}\cdots CO^{I}$$

are considered in addition to the MMCT ($CO^{II}\cdots CO^{III}\cdots CO^{II} \rightarrow CO^{III}\cdots CO^{II}\cdots CO^{I}$) and ones between the Co(II) centers together with all the involved on-site LF and LMCT transitions involving the local Co(II) tetrahedral and Co(III) octahedral centers, the computed bands are systematically converged to their experimental counterparts.

Deconvolution of the computed band gaps using the CAS(26,20) active space reveals that ligand field (LF) transitions localized at the tetrahedral Co(II) sites are present in all cases and provide the fundamental basis for the optical gaps. The differences in character between the individual gaps arise from varying degrees of correlation-driven mixing with metal-to-metal (MMCT/M'MCT/MM'CT) and ligand-to-metal (LMCT) charge transfer excitations.

The low-energy transition in the CAS(26,20) model located at 0.78 eV arises primarily from LF excitations localized at the
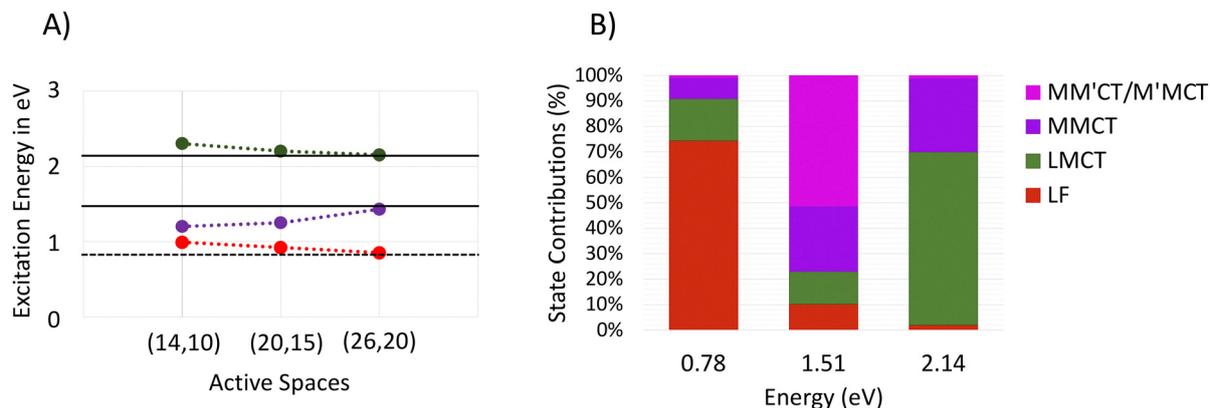
Fig. 8 (A) CAS-ICE/NEVPT2 computed BGs for increasing active spaces to include, in addition to the CoII-center-based orbitals in model 2t4o (consisting a CAS(14,10)) a sequence of increasing active spaces consisting of the respective Co(III)-based orbitals arising from one (CAS(20,15)), and two (CAS(26,20)), Co(III) centers. (B) Deconvolution of the computed band gaps employing active space CAS(20,15) in terms of LF, LMCT, MMCT and MM'CT/ M'MCT contributions.

tetrahedral Co(II) centers, consistent with the behavior observed previously in the isolated-site (1t) models. Although this transition is formally dipole-allowed and thus, by convention referred to as the first optical band gap, its extremely low oscillator strength ($f < 10^{-6}$) makes it practically insignificant for absorption, in agreement with experimental observations.

In the CAS(26,20) model, the transition located at 1.51 eV, corresponding to the central experimental band gap of Co_3O_4, arises from LF excitations at the tetrahedral Co(II) centers that are strongly mixed with MMCT and M'MCT/MM'CT components along with a minor contribution from LMCT transitions. This excitation carries significantly higher oscillator strength compared to the 0.78 eV transition and thus defines the principal optical band gap of Co_3O_4.

While this model decomposes the 1.51 eV transition into these different components, comparison with broken-symmetry TD-DFT and MR-EOM-CC isolated-site results suggests a more nuanced picture. Part of the apparent MMCT/M'MCT/MM'CT characteristic likely reflects correlation-driven mixing of local 'neutral' (Co(II)) and 'ionic' (Co(I)/Co(III)) antiferromagnetic configurations at the tetrahedral centers. Although a minor ligand field contribution from neutral Co(II) sites is apparent in the CAS(26,20) calculations, the dominant character involves excitations arising from partially 'ionic' states. Rather than representing pure inter-site electron transfer, these mixed configurations enable ligand field-like excitations to access the energy range of the central optical gap. This interpretation highlights the essential role of dynamic electron correlation in reorganizing the local electronic structure to give rise to the experimentally observed optical band gap.

In the CAS(26,20) model, the transition located at 2.13 eV arises from ligand field (LF) excitations at tetrahedral Co(II) centers that are strongly mixed with ligand-to-metal charge transfer (LMCT) components, along with a smaller admixture of MMCT character. This excitation carries higher oscillator strength compared to the 1.51 eV transition, consistent with the stronger absorption onset observed experimentally. This is all summarized in Table 4 and Fig. 9.

It should be emphasized that all three experimentally observed band gaps in Co_3O_4 originate from on-site ligand field transitions at the Co(II) tetrahedral sites, and these provide the fundamental electronic characteristics of the respective excitations. However, as correlation effects are introduced (e.g., at the NEVPT2 level), these LF states increasingly mix with charge transfer (CT) configurations, especially metal-to-metal (MMCT) and ligand-to-metal (LMCT), through configuration interaction. This mixing redistributes the oscillator strength and leads to the partial CT character reflected in the decomposition shown in Table 4. Overall, the analysis reveals that the three band gap energies correspond to excitations that are of fundamentally ligand field origin, but with increasing degrees of mixing with CT configurations depending on the energy and the specific manifold of excited states involved.

IX. Conclusions

In this work, the fundamental band gap problem of Co_3O_4 was revisited. In an effort to shed light on the origins of the three experimentally observed band gaps in Co_3O_4, which are located at 0.78 eV, 1.51 eV, and 2.14 eV, a systematic electrostatic embedding

Table 4 Numerical evaluation employing a Hubbard like model Hamiltonian to a set of chosen CSFs to represent the predominant d–d, MMCT and LMCT transitions

Experimental BGs	(26,20) SA-CASSCF/NEVPT2	BG character	State mixing
0.78	0.78	LF ('neutral')	75%LF + 15%LMCT + 5%M'MCT/MM'CT
1.52	1.51	LF + MMCTs ('ionic')	12%LF + 7%LMCT + 31%MMCT + 50%M'MCT/MM'CT
2.11	2.13	LF + LMCT ('neutral')	2%LF + 75%LMCT + 15%MMCT

This journal is © the Owner Societies 2025
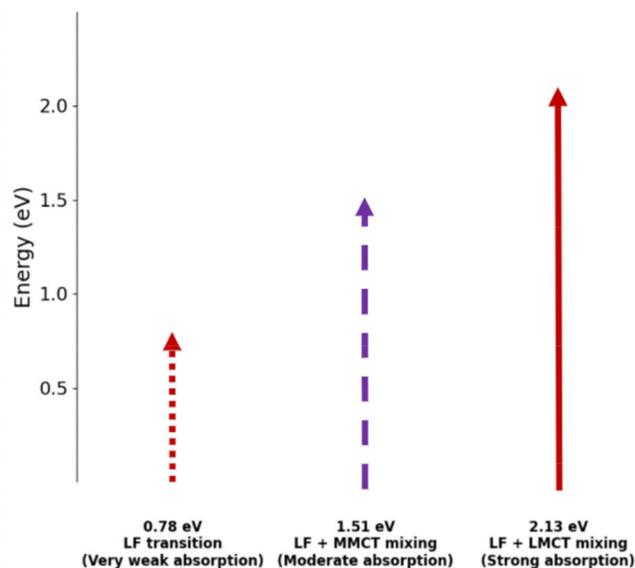
Phys. Chem. Chem. Phys., 2025, **27**, 17225–17244 | **17239**

Fig. 9 Schematic representation of the optical transitions in Co_3O_4. Arrows indicate the observed transitions at 0.78 eV, 1.51 eV, and 2.13 eV corresponding to the experimentally observed band gaps. Red: dominantly 'neutral' states, purple: dominantly 'ionic' states. The lines qualitatively reflect oscillator strength: dotted corresponds to weaker, dashed to moderate, and solid lines to stronger absorption.

computational protocol was employed. To disentangle the site-specific electronic contributions of Co(II) and Co(III), the isostructural derivatives $Al_2Co(II)O_4$ and $Co(III)_2ZnO_4$ are also considered, each selectively retaining either the tetrahedral Co(II) or the octahedral Co(III) centers. All relevant direct optical excitations were computed using both TD-DFT and wavefunction-based correlated methods. The application of various computational methods allowed for cross-validation of the results. In particular, the electrostatic embedding approach enabled the modelling of distinct regions of the material, helping to isolate specific excitations at individual cobalt oxide sites. To address the problem at hand, a range of model sizes were employed, allowing for the use of wavefunction-based methods with increasing accuracy. Among these, CASSCF, CASSCF/NEVPT2, and MR-EOM-CC were utilized to reliably reproduce the experimental values.

This approach enabled us to systematically analyze both the number and nature of the three experimental band gaps. As a first step, starting from a 2t4o model and treating the 'neutral' and 'ionic' ligand field excited states separately, we found that while the 'neutral' ligand field excited states fall within the energy range of the three experimental band gaps, it is only when electron correlation is accounted for at the NEVPT2 level that the 'ionic' ligand field states also align with these energy regions. Using reduced models, we identified the origin of all three band gaps, linking them to ligand field transitions at tetrahedral Co sites. In the 'neutral' antiferromagnetic ground state, where all tetrahedral Co sites are Co(II) A-site centers ($3d^7$), ligand field transitions occur at 0.78 eV and 2.14 eV. In contrast, 'ionic' ligand field transitions across A–A′ sites suggest the presence of Co(I) ($3d^8$) or Co(III) ($3d^6$) centers, leading to transitions that correspond to the low- and middle-energy band gaps.

To investigate the influence of electron localization and correlation on band gap energies, we revisited the Hubbard Hamiltonian within the Born–Oppenheimer framework. In this context, we numerically evaluated key terms to estimate the energies of ligand field (LF), LMCT, and MMCT transitions using 'bare' one- and two-electron CASSCF integrals, incorporating electron correlation through a reduction factor applied to Coulomb repulsion integrals, derived from NEVPT2 stabilization of 'neutral' and 'ionic' state energies relative to CASSCF. While simplistic, this numerical approach offers valuable insights into the three band gap transitions, particularly highlighting the role of electron correlation in shaping the middle band gap energy. The state-mixing mechanism extends beyond a simple integral reduction, requiring a simultaneous and explicit treatment of all interactions.

Seeking further validation, CAS-ICE/NEVPT2 calculations were performed on all possible 'neutral' and 'ionic' excited states originating the 'neutral' antiferromagnetic ground state by systematically increasing active spaces from CAS(14,10) to CAS(20,15) and CAS(26,20). This approach captured key on-site and inter-site interactions between tetrahedral Co(II) and octahedral Co(III) centers in the 2t4o model. As the active space increased, the most intense computed bands converged to experimental band gap values, confirming that while all three band gaps have an essential on-site ligand field character localized on Co(II), they are fundamentally distinct. The lowest energy transition at 0.78 eV corresponds to an on-site LF transition, associated with charge transport and redox properties. The middle-energy band gap at 1.51 eV arises from a mix of on-site LF and inter-site MMCT transitions, representing the optical band gap of Co_3O_4, which directly impacts photocatalytic activity and surface reactivity. Finally, the high-energy band gap at 2.13 eV, composed of both on-site LF and LMCT transitions, corresponds to the semiconductive band gap, influencing the material's thermal conductivity.

We believe that the results presented herein are essential for designing cobalt oxide catalysts with tailored optical properties. Our efforts are currently on-going with an aim to understand the electronic structure properties of Co_3O_4 that may be probed by vibrational, as well as a variety of X-ray spectroscopy techniques.

Conflicts of interest

There are no conflicts to declare.

Data availability

Literature and analysis tables together with discussions regarding the impact of electron correlation to the excited states as well as to the magnetic ground state of Co3O4 along with representative inputs are provided in the ESI.†

Acknowledgements

17240 | *Phys. Chem. Chem. Phys.*, 2025, **27**, 17225–17244

This journal is © the Owner Societies 2025

References

1 P. Mountapmbeme Kouotou, H. Vieker, Z. Y. Tian, P. H. Tchoua Ngamou, A. El Kasmi, A. Beyer, A. Gölzhäuser and K. Kohse-Höinghaus, *Catal. Sci. Technol.*, 2014, **4**, 3359.

2 X. Xie, Y. Li, Z. Q. Liu, M. Haruta and W. Shen, *Nature*, 2009, **458**, 746.

3 J. Thomas, N. Thomas, F. Girgsdies, M. Beherns, X. Huang, V. D. Sudheesh and V. Sebastian, *New J. Chem.*, 2017, **41**, 7356.

4 G. Evans, I. V. Kozhevnikov, E. F. Kozhevnikova, J. B. Claridge, R. Vaidhyanathan, C. Dickinson, C. D. Wood, A. I. Cooper and M. J. Rosseinsky, *J. Mater. Chem.*, 2008, **18**, 5518.

5 C. A. Chagas, E. F. D. Souza, M. C. N. A. D. Carvalho, R. L. Martins and M. Schmal, *Appl. Catal., A*, 2016, **519**, 139.

6 L. Lukashuk, K. Föttinger, E. Kolar, C. Rameshan, D. Teschner, M. Hävecker, A. Knop-Gericke, N. Yigit, H. Li, E. McDermott, M. Stöger-Pollach and G. Rupprechter, *J. Catal.*, 2016, **344**, 1.

7 N. Bahlawane, P. H. T. Ngamou, V. Vannier, T. Kottke, J. Heberle and K. Kohse-Hoinghaus, *Phys. Chem. Chem. Phys.*, 2009, **11**, 9224.

8 Z. Y. Tian, P. Mountapmbeme Kouotou, A. El Kasmi, P. H. Tchoua Ngamou, K. Kohse-Höinghaus, H. Vieker, A. Beyer and A. Gölzhäuser, *Proc. Combust. Inst.*, 2015, **35**, 2207.

9 Z. Y. Tian, P. H. Tchoua Ngamou, V. Vannier, K. Kohse-Höinghaus and N. Bahlawane, *Appl. Catal., B*, 2012, **117–118**, 125.

10 K. F. Ortega, S. Anke, S. Salamon, F. Özcan, J. Heese, C. Andronescu, J. Landers, H. Wende, W. Schuhmann, M. Muhler, T. Lunkenbein and M. Behrens, *Chem. – Eur. J.*, 2017, **23**, 12443.

11 S. Zafeiratos, T. Dintzer, D. Teschner, R. Blume, M. Hävecker, A. Knop-Gericke and R. Schlögl, *J. Catal.*, 2010, **269**, 309.

12 S. Anke, G. Bendt, I. Sinev, H. Hajiyani, H. Antoni, I. Zegkinoglou, H. Jeon, R. Pentcheva, B. Roldan Cuenya, S. Schulz and M. Muhler, *ACS Catal.*, 2021, **9**(7), 5974–5985.

13 V. R. Mate, M. Shirai and C. V. Rode, *Catal. Commun.*, 2013, **33**, 66–69.

14 X. Xiao, X. Liu, H. Zhao, D. Chen, F. Liu, J. Xiang, Z. Hu and Y. Li, *Adv. Mater.*, 2012, **24**, 5762–5766.

15 J. Liu, J. Jiang, C. Cheng, H. Li, J. Zhang, H. Gong and H. J. Fan, *Adv. Mater.*, 2011, **23**, 2076–2081.

16 X. W. Lou, D. Deng, J. Y. Lee, J. Feng and L. A. Archer, *Adv. Mater.*, 2008, **20**, 258–262.

17 Y. Liang, Y. Li, H. Wang, J. Zhou, J. Wang, T. Regier and H. Dai, *Nat. Mater.*, 2011, **10**, 780–786.

18 F. Jiao and H. Frei, *Angew. Chem., Int. Ed.*, 2009, **48**, 1841–1844.

19 J. Wu, Y. Xue, X. Yan, W. Yan, Q. Cheng and Y. Xie, *Nano Res.*, 2012, **5**, 521–530.

20 A. Gasparotto, D. Barreca, D. Bekermann, A. Devi, R. A. Fischer, P. Fornasiero, V. Gombac, O. I. Lebedev, C. Maccato, T. Montini, G. Van Tendeloo and E. Tondello, *J. Am. Chem. Soc.*, 2011, **133**, 19362–19365.

21 Y. Wu, S. Ruirui and J. Cen, *Front. Chem.*, 2020, **8**, 386.

22 M. D. Kärkäs, O. Verho, E. V. Johnston and B. Åkermark, *Chem. Rev.*, 2014, **114**, 11863–12001.

23 J. Ma, H. Wei, Y. Liu, X. Ren, Y. Li, F. Wang, X. Han, E. Xu, X. Cao, G. Wang, F. Ren and S. Wei, *Int. J. Hydrogen Energy*, 2020, **45**, 21205–21220.

24 B. Kupfer, K. Majhi, D. A. Keller, Y. Bouhadana, S. Rühle, H. N. Barad, A. Y. Anderson and A. Zaban, *Adv. Energy Mater.*, 2014, **5**, 1401007.

25 K. Majhi, L. Bertoluzzi, K. J. Rietwyk, A. Ginsburg, D. A. Keller, P. Lopez-Varo, A. Y. Anderson, J. Bisquert and A. Zaban, *Adv. Mater. Interfaces*, 2015, **3**, 1500405.

26 Y. Zhang, J. Ge, B. Mahmoudi, S. Förster, F. Syrowatka, A. W. Maijenburg and R. Scheer, *ACS Appl. Energy Mater.*, 2020, **3**, 3755–3769.

27 B. Ge, Z. R. Zhou, X. F. Wu, L. R. Zheng, S. Dai, A. P. Chen, Y. Hou, H. G. Yang and S. Yang, *Adv. Funct. Mater.*, 2021, **31**, 2106121.

28 K. Majhi, L. Bertoluzzi, D. A. Keller, H. N. Barad, A. Ginsburg, A. Y. Anderson, R. Vidal, P. Lopez-Varo, I. Mora-Sero, J. Bisquert and A. Zaban, *J. Phys. Chem. C*, 2016, **120**, 9053–9060.

29 L. Qiao, H. Y. Xiao, H. M. Meyer, J. N. Sun, C. M. Rouleau, A. A. Puretzky, D. B. Geohegan, I. N. Ivanov, M. Yoon, W. J. Weber and M. D. Biegalski, *J. Mater. Chem. C*, 2013, **1**, 4628–4633.

30 J.-L. Bredas, *Mater. Horiz.*, 2014, **1**, 17–19.

31 K. P. Reddy, R. Jain, M. K. Ghosalya and C. S. Gopinath, *J. Phys. Chem. C*, 2017, **121**, 21472–21481.

32 C.-S. Cheng, M. Serizawa, H. Sakata and T. Hirayma, *Mater. Chem. Phys.*, 1998, **53**, 225–230.

33 D. Barreca, C. Massignan, S. Daolio, M. Fabrizio, C. Piccirillo, L. Armelao and E. Tondello, *Chem. Mater.*, 2001, **13**, 588–593.

34 H. Yamamoto, S. Tanaka and K. Hirao, *J. Appl. Phys.*, 2003, **93**, 4158–4162.

35 N. Bahlawane, E. Fischer Rivera, K. Kohse-Höinghaus, A. Brechling and U. Kleineberg, *Appl. Catal., B*, 2004, **53**, 245–255.

36 S. Thota, A. Kumar and J. Kumar, *Mater. Sci. Eng., B*, 2009, **164**, 30–37.

37 M. M. Waegle, H. Q. Doan and T. Cuk, *J. Phys. Chem. C*, 2014, **118**, 3426–3432.

38 C.-M. Jiang, L. R. Baker, J. M. Lucas, J. Vura-Weis and A. P. Alivisatos, *J. Phys. Chem. C*, 2014, **118**, 22774–22784.

39 W. A. Murad, S. M. Al-Shamari, F. H. Al-Khateeb and R. H. Misho, *Phys. Status Solidi A*, 1988, **106**, 143–146.

40 L. Schumacher, I. B. Holzhueter, I. R. Hill and M. J. Dignam, *Electrochim. Acta*, 1990, **35**, 975–984.

41 A. J. Varkey and A. F. Fort, *Sol. Energy Mater. Sol. Cells*, 1993, **31**, 277–282.

This journal is © the Owner Societies 2025

Phys. Chem. Chem. Phys., 2025, **27**, 17225–17244 | **17241**

42 P. S. Patil, L. D. Kadam and C. D. Lokhande, *Thin Solid Films*, 1996, **272**, 29–32.

43 L. D. Kadam and P. S. Patil, *Mater. Chem. Phys.*, 2001, **68**, 225–232.

44 B. Pejova, A. Isahi, M. Najdoski and I. Grozdanov, *Mater. Res. Bull.*, 2001, **36**, 161–170.

45 A. U. Mane and S. A. Shivashankar, *J. Cryst. Growth*, 2003, **254**, 368–377.

46 A. Gulino, G. Fiorito and I. Fragalà, *J. Mater. Chem.*, 2003, **13**, 861–865.

47 V. R. Shinde, S. B. Mahadik, T. P. Gujar and C. D. Lokhande, *Appl. Surf. Sci.*, 2006, **252**, 7487–7492.

48 P. H. T. Ngamou and N. Bahlawane, *Chem. Mater.*, 2010, **22**, 4158–4165.

49 A. Louradi, A. Rmili, F. Ouachtrai, A. Couaoud, B. Elidrissi and H. Erguig, *J. Alloys Compd.*, 2011, **509**, 9183–9189.

50 A. Lakehal, B. Bedhiaf, A. Bouaza, H. Benhebal, A. Ammari and C. Dalache, *Mater. Res.*, 2018, **21**, e20170545.

51 A. E. Cherkashin and F. I. Vilesov, *Sov. Phys. Solid State*, 1969, **11**, 1068.

52 I. D. Belova, Y. E. Roginskaya, R. R. Shifrina, S. G. Oagarin, Y. V. Plekhanov and Y. N. Venevtsev, *Solid State Commun.*, 1983, **47**, 577–584.

53 J. W. D. Martens, W. L. Peeters and H. M. van Noort, *J. Phys. Chem. Solids*, 1985, **46**, 411–416.

54 J. G. Cook and M. P. van der Meer, *Thin Solid Films*, 1986, **144**, 165–176.

55 M. Lenglet and C. K. Jørgensen, *Chem. Phys. Lett.*, 1994, **229**, 616–620.

56 P. Nkeng, G. Poillerat, J. F. Koenig, P. Chartier, B. Lefez, J. Lopitaux and M. Lenglet, *J. Electrochem. Soc.*, 1995, **142**, 1777–1783.

57 P. Ruzakowski Athey, F. K. Urban III, M. F. Tabet and W. A. McGahan, *J. Vac. Sci. Technol., A*, 1996, **14**, 685–692.

58 S. R. Gawali, A. C. Gandhi, S. S. Gaikwad, J. Pant, T.-S. Chan, C.-L. Cheng, Y.-R. Ma and S. Y. Wu, *Sci. Rep.*, 2018, **8**, 249.

59 S. A. Makhlouf, *J. Magn. Magn. Mater.*, 2002, **246**, 184–190.

60 W. L. Roth, *J. Phys. Chem. Solids*, 1964, **25**, 1–10.

61 T. Böhland, K. Brandt, H. Brussaard, D. Calvert, G. Etzrodt, H. Rieck, O. Seeger, H. Wienand, J. Wiese and G. Buxbaum, *Ind. Inorg. Pigm.*, 2005, 99–162.

62 N. H. Perry, T. O. Mason, C. Ma, A. Navrotsky, Y. Shi, J. S. Bettinger, M. F. Toney, T. R. Paudel, S. Lany and A. Zunger, *J. Solid State Chem.*, 2012, **190**, 143–149.

63 L. Chen, F. Hu, H. Duan, Q. Liu, H. Tan, W. Yan, T. Yao, Y. Jiang, Z. Sun and S. Wei, *Appl. Phys. Lett.*, 2016, **108**, 252402.

64 T. Kanazawa, K. Kato, R. Yamaguchi, T. Uchiyama, D. L. Lu, S. Nozawa, A. Yamakata, Y. Uchimoto and K. Maeda, *ACS Catal.*, 2020, **10**, 4960–4966.

65 F. Rong, J. Zhao, P. P. Su, Y. Yao, M. R. Li, Q. H. Yang and C. Li, *J. Mater. Chem. A*, 2015, **3**, 4010–4017.

66 M. Shepit, V. K. Paidi, C. A. Roberts and J. van Lierop, *Sci. Rep.*, 2020, **10**, 20990.

67 W. H. Ji, L. Yin, W. M. Zhu, C. M. N. Kumar, C. Li, H. F. Li, W. T. Jin, S. Nandi, X. Sun, Y. Su, T. Brückel, Y. Lee, B. N. Harmon, L. Ke, Z. W. Ouyang and Y. Xiao, *Phys. Rev. B*, 2019, **100**, 134420.

68 K. Pal, S. Dey, A. Alam and I. Das, *Sci. Rep.*, 2024, **14**, 30678.

69 I. Dzyaloshinsky, *J. Phys. Chem. Solids*, 1958, **4**, 241–255.

70 T. Moriya, *Phys. Rev.*, 1960, **120**, 91–98.

71 S. Kim, S. Pathak, S. H. Rhim, J. Cha, S. Jekal, S. C. Hong, H. H. Lee, S.-H. Park, H.-K. Lee, J.-H. Park, S. Lee, H.-G. Steinrück, A. Mehta, S. X. Wang and J. Hong, *Adv. Sci.*, 2022, **9**, 2201749.

72 A. Cadi-Essadeka, A. Roldana, D. Santos-Carballala, P. E. Ngoepeb, M. Claeysc and N. H. de Leeuw, *S. Afr. J. Chem.*, 2021, **74**, 8–16.

73 L. Wang, T. Maxisch and G. Ceder, *Phys. Rev. B: Condens. Matter Mater. Phys.*, 2006, **73**, 195107.

74 A. Montoya and B. S. Haynes, *Chem. Phys. Lett.*, 2011, 63–68.

75 V. Singh, M. Kosa, K. Majhi and D. T. Major, *J. Chem. Theory Comput.*, 2015, **11**, 64–72.

76 O. M. Sousa, J. S. Lima, A. F. Lima and M. V. Lalic, *J. Magn. Magn. Mater.*, 2019, **484**, 21–30.

77 V. S. Zhandun and A. Nemtsev, *J. Magn. Magn. Mater.*, 2020, **499**, 166306.

78 G. A. Kaptagay, T. M. Inerbaeva, Y. A. Mastrikovb, E. A. Kotominb and A. T. Akilbekova, *Solid State Ionics*, 2015, **277**, 77–82.

79 A. F. Lima, *J. Phys. Chem. Solids*, 2016, **91**, 86–89.

80 X.-L. Xu, Z.-H. Chen, Y. Li, W.-K. Chen and J.-Q. Li, *Surf. Sci.*, 2009, **603**, 653–658.

81 J. Chen, X. Wu and A. Selloni, *Phys. Rev. B: Condens. Matter Mater. Phys.*, 2011, **83**, 245204.

82 A. F. Lima, *J. Phys. Chem. Solids*, 2014, **75**, 148–152.

83 A. Walsh, S.-H. Wei, Y. Yan, M. M. Al-Jassim, J. A. Turner, M. Woodhouse and B. A. Parkinson, *Phys. Rev. B: Condens. Matter Mater. Phys.*, 2007, **76**, 165119.

84 N. H. M. Zaki, M. Mustaffa, M. F. M. Taib, O. H. Hassan, M. Z. A. Yahya and A. M. M. Ali, *Int. J. Eng. Technol.*, 2018, **7**, 121–125.

85 J. P. Perdew, *Int. J. Quantum Chem.*, 1986, **19**, 497–523.

86 A. J. Garza and G. E. Scuseria, *J. Phys. Chem. Lett.*, 2016, **7**, 4165–4170.

87 J. Heyd, J. E. Peralta, G. E. Scuseria and R. L. Martin, *J. Chem. Phys.*, 2005, **123**, 174101.

88 J. P. Perdew, W. Yang, K. Burke, Z. Yang, E. K. U. Gross, M. Scheffler, G. E. Scuseria, T. M. Henderson, I. Y. Zhang, A. Ruzsinszky, H. Peng, J. Sun, E. Trushin and A. Görling, *Proc. Natl. Acad. Sci. U. S. A.*, 2017, **114**, 2801–2806.

89 J. P. Perdew and A. Ruzsinszky, *Eur. Phys. J. B*, 2018, **91**, 108.

90 A. Dittmer, R. Izsák, F. Neese and D. Maganas, *Inorg. Chem.*, 2019, **58**, 9303–9315.

91 T. Helgaker, S. Coriani, P. Jørgensen, K. Kristensen, J. Olsen and K. Ruud, *Chem. Rev.*, 2012, **112**, 543–631.

92 A. Dittmer, G. L. Stoychev, D. Maganas, A. A. Auer and F. Neese, *J. Chem. Theory Comput.*, 2020, **16**, 6950–6967.

93 A. Kubas, D. Berger, H. Oberhofer, D. Maganas, K. Reuter and F. Neese, *J. Phys. Chem. Lett.*, 2016, **7**, 4207–4212.

17242 | *Phys. Chem. Chem. Phys.*, 2025, **27**, 17225–17244

This journal is © the Owner Societies 2025

94 R. Shafei, D. Maganas, P. J. Strobel, P. J. Schmidt, W. Schnick and F. Neese, *J. Am. Chem. Soc.*, 2022, **144**, 8038–8053.

95 D. Stodt, H. Noei, C. Hattig and Y. Wang, *Phys. Chem. Chem. Phys.*, 2013, **15**, 466–472.

96 A. D. Boese and J. Sauer, *Phys. Chem. Chem. Phys.*, 2013, **15**, 16481–16493.

97 M. Pöhlchen and V. Staemmler, *J. Chem. Phys.*, 1992, **97**, 2583–2592.

98 F. Libisch, C. Huang and E. A. Carter, *Acc. Chem. Res.*, 2014, **47**, 2768.

99 G. Kotliar, S. Y. Savrasov, K. Haule, V. S. Oudovenko, O. Parcollet and C. A. Marianetti, *Rev. Mod. Phys.*, 2006, **78**, 865.

100 Q. Sun and G. K. L. Chan, *Acc. Chem. Res.*, 2016, **49**, 2705.

101 M. Olejniczak, R. Bast and A. S. Pereira Gomes, *Phys. Chem. Chem. Phys.*, 2017, **19**, 8400–8415.

102 C. R. Jacob and L. Visscher, *J. Chem. Phys.*, 2006, **125**, 194104.

103 T. A. Wesolowski, S. Shedge and X. Zhou, *Chem. Rev.*, 2015, **115**, 5891–5928.

104 J. D. Hartman, A. Balaji and G. J. O. Beran, *J. Chem. Theory Comput.*, 2017, **13**, 6043–6051.

105 J. Chen, X. Wu and A. Selloni, *Phys. Rev. B: Condens. Matter Mater. Phys.*, 2011, **83**, 245204.

106 M. Shepit, V. K. Paidi, C. A. Roberts and J. van Lierop, *Sci. Rep.*, 2020, **10**, 20990.

107 C. L. Benavides-Riveros, N. N. Lathiotakis and M. A. L. Marques, *Phys. Chem. Chem. Phys.*, 2017, **19**, 12655–12664.

108 E. Morosan, D. Natelson, A. H. Nevidomskyy and Q. Si, *Adv. Mater.*, 2012, **24**, 4896–4923.

109 Y. A. Izyumov and E. Z. Kurmaev, *Phys.*, 2008, **51**, 23–56.

110 J. M. Crowley, J. Tahir-Kheli and W. A. Goddard, *J. Phys. Chem. Lett.*, 2016, **7**, 1198–1203.

111 B. O. Roos, P. R. Taylor and P. E. M. Sigbahn, *Chem. Phys.*, 1980, **48**, 157–173.

112 B. O. Roos, *Int. J. Quantum Chem.*, 1980, **14**, 175–189.

113 P. E. M. Sigbahn, J. Almlöf, A. Heiberg and B. O. Roos, *J. Chem. Phys.*, 1981, **74**, 2384–2396.

114 C. Angeli, R. Cimiraglia, S. Evangelisti, T. Leininger and J.-P. Malrieu, *J. Chem. Phys.*, 2001, **114**, 10252–10264.

115 C. Angeli, R. Cimiraglia and J.-P. Malrieu, *Chem. Phys. Lett.*, 2001, **350**, 297–305.

116 C. Angeli, R. Cimiraglia and J.-P. Malrieu, *J. Chem. Phys.*, 2002, **117**, 9138–9153.

117 S. Sharma and G. K.-L. Chan, *J. Chem. Phys.*, 2012, **136**, 124121.

118 V. G. Chilkuri and F. Neese, *J. Comput. Chem.*, 2021, **42**, 982–1005.

119 V. G. Chilkuri and F. Neese, *J. Chem. Theory Comput.*, 2021, **17**, 2868–2885.

120 G. Li Manni, S. D. Smart and A. Alavi, *J. Chem. Theory Comput.*, 2016, **12**, 1245–1258.

121 S. Sharma, K. Sivalingam, F. Neese and G. K.-L. Chan, *Nat. Chem.*, 2014, **6**, 927–933.

122 A. Lunghi and F. Totti, *Inorganics*, 2016, **4**, 28.

123 V. G. Chilkuri, S. DeBeer and F. Neese, *Inorg. Chem.*, 2020, **59**, 984–995.

124 W. Dobrautz, O. Weser, N. A. Bogdanov, A. Alavi and G. Li Manni, *J. Chem. Theory Comput.*, 2021, **17**, 5684–5703.

125 K. Andersson, P.-Å. Malmqvist, B. O. Roos, A. J. Sadlej and K. Wolinski, *J. Phys. Chem.*, 1990, **94**, 5483–5488.

126 K. Andersson, P.-A. Malmqvist and B. O. Roos, *J. Phys. Chem.*, 1992, **96**, 1218–1226.

127 M. Nooijen, O. Demel, D. Datta, L. G. Kong, K. R. Shamasundar, V. Lotrich, L. M. Huntington and F. Neese, *J. Chem. Phys.*, 2014, **140**, 081102.

128 A. Sugie, K. Nakano, K. Tajima, I. Osaka and H. Yoshida, *J. Phys. Chem. Lett.*, 2023, **14**, 11412–11420.

129 Y. Zhu, F. Zhao, W. Wang, Y. Li, S. Zhang and Y. Lin, *Adv. Energy Sustainability Res.*, 2022, **3**, 2100184.

130 H. Zhong, F. Pan, S. Yue, C. Qin, V. Hadjiev, F. Tian, X. Liu, F. Lin, Z. Wang and J. Bao, *J. Phys. Chem. Lett.*, 2023, **14**, 6702–6708.

131 T. Tanaka, *Jpn. J. Appl. Phys.*, 1979, **18**, 1043–1047.

132 K. J. Kim and Y. R. Park, *Solid State Commun.*, 2003, **127**, 25–28.

133 K. J. Kim and Y. R. Park, *Solid State Commun.*, 2003, **127**, 25–28.

134 T. Tanaka, *Jpn. J. Appl. Phys.*, 1979, **18**, 1043–1047.

135 S. Thota, A. Kumar and J. Kumar, *Mater. Sci. Eng., B*, 2009, **164**, 30–37.

136 B. Pejova, A. Isahi, M. Najdoski and I. Grozdanov, *Mater. Res. Bull.*, 2001, **36**, 161–170.

137 D.-K. Seo and R. Hoffmann, *Theor. Chem. Acc.*, 1999, **102**, 23–32.

138 K. M. E. Miedzinska, B. R. Hollebone and J. G. Cook, *J. Phys. Chem. Solids*, 1987, **48**, 649–656.

139 K. M. E. Miedzinska, B. R. Hollebone and J. G. Cook, *J. Phys. Chem. Solids*, 1987, **48**, 649–656.

140 J. P. Perdew, *Phys. Rev. B: Condens. Matter Mater. Phys.*, 1986, **33**, 8822–8824.

141 F. Neese, *Wiley Interdiscip. Rev.: Comput. Mol. Sci.*, 2012, **2**, 73–78.

142 F. Neese, F. Wennmohs, U. Becker and C. Riplinger, *J. Chem. Phys.*, 2020, **152**, 224108.

143 F. Neese, *Wiley Interdiscip. Rev.: Comput. Mol. Sci.*, 2018, **8**, e1327.

144 F. Neese, *Wiley Interdiscip. Rev.: Comput. Mol. Sci.*, 2022, **12**, e1606.

145 F. Neese, *Faraday Discuss.*, 2024, **254**, 295–314.

146 J. P. Perdew, K. Burke and M. Ernzerhof, *Phys. Rev. Lett.*, 1996, **77**, 3865.

147 C. Adamo and V. Barone, *J. Chem. Phys.*, 1999, **110**, 6158–6169.

148 M. Douglas and N. M. Kroll, *Ann. Phys.*, 1974, **82**(1), 89–155.

149 M. Barysz and A. J. Sadlej, *THEOCHEM*, 2001, **573**, 181–200.

150 R. J. Bartlett, *Wiley Interdiscip. Rev.: Comput. Mol. Sci.*, 2012, **2**, 126–138.

151 R. J. Bartlett and M. Musiał, *Rev. Mod. Phys.*, 2007, **79**, 291–352.

This journal is © the Owner Societies 2025

Phys. Chem. Chem. Phys., 2025, **27**, 17225–17244 | **17243**

152 M. Nooijen and R. J. Bartlett, *J. Chem. Phys.*, 1997, **107**, 6812–6830.

153 A. D. Becke, *Phys. Rev. A: At., Mol., Opt. Phys.*, 1988, **38**, 3098–3100.

154 J. P. Perdew, K. Burke and M. Ernzerhof, *Phys. Rev. Lett.*, 1996, **77**, 3865.

155 J. M. Tao, J. P. Perdew, V. N. Staroverov and G. E. Scuseria, *Phys. Rev. Lett.*, 2003, **91**, 146401.

156 J. G. Brandenburg, C. Bannwarth, A. Hansen and S. Grimme, *J. Chem. Phys.*, 2018, **148**, 064104.

157 C. Lee, W. Yang and R. G. Parr, *Phys. Rev. B: Condens. Matter Mater. Phys.*, 1988, **37**, 785.

158 S. Grimme, A. Hansen, S. Ehlert and J.-M. Mewes, *J. Chem. Phys.*, 2021, **154**, 064103.

159 J. P. Perdew, J. A. Chevary, S. H. Vosko, K. A. Jackson, M. R. Pederson, D. J. Singh and C. Fiolhais, *Phys. Rev. B: Condens. Matter Mater. Phys.*, 1992, **46**, 6671–6687.

160 A. D. Becke, *J. Chem. Phys.*, 1993, **98**, 5648.

161 J. P. Perdew, J. Tao, V. N. Staroverov and G. E. Scuseria, *J. Chem. Phys.*, 2004, **120**, 6898–6911.

162 S. Kozuch and J. M. L. Martin, *Phys. Chem. Chem. Phys.*, 2011, **13**, 20104–20107.

163 M. Casanova-Páez and L. Goerigk, *J. Chem. Theory Comput.*, 2021, **17**, 5165–5186.

164 S. Grimme, *J. Chem. Phys.*, 2006, **124**, 034108.

165 M. Casanova-Páez, M. B. Dardis and L. Goerigk, *J. Chem. Theory Comput.*, 2019, **15**, 4735–4744.

166 S. Kozuch, D. Gruzman and J. M. L. Martin, *J. Phys. Chem. C*, 2010, **114**, 20801–20808.

167 S. Kozuch and J. M. L. Martin, *J. Comput. Chem.*, 2013, **34**, 2327–2344.

168 S. Pathak, L. Lang and F. Neese, *J. Chem. Phys.*, 2017, **147**, 234109.

169 F. Weigend and R. Ahlrichs, *Phys. Chem. Chem. Phys.*, 2005, **7**, 3297–3305.

170 D. Aravena, F. Neese and D. A. Pantazis, *J. Chem. Theory Comput.*, 2016, **12**, 1148–1156.

171 T. H. Dunning, *J. Chem. Phys.*, 1989, **90**, 1007–1023.

172 D. Liakos and F. Neese, *J. Phys. Chem. A*, 2012, **116**, 4801–4816.

173 G. Orlandi and W. Siebrand, *Chem. Phys. Lett.*, 1972, **15**, 465–468.

174 D. Maganas, J. K. Kowalska, C. Van Stappen, S. DeBeer and F. Neese, *J. Chem. Phys.*, 2019, **152**, 114107.

175 D. Ganyushin and F. Neese, *J. Chem. Phys.*, 2008, **128**, 114117.

176 M. Atanasov, D. Aravena, E. Suturina, E. Bill, D. Maganas and F. Neese, *Coord. Chem. Rev.*, 2015, **289–290** 177–214.

177 T. Leyser da Costa Gouveia, D. Maganas and F. Neese, *J. Phys. Chem. A*, 2024, **128**, 5041–5053.

178 R. Shafei, A. Hamano, C. Gourlaouen, D. Maganas, K. Takano, C. Daniel and F. Neese, *J. Chem. Phys.*, 2023, **159**, 084102.

179 R. Shafei, P. J. Strobel, P. J. Schmidt, D. Maganas, W. Schnick and F. Neese, *J. Phys. Chem. C*, 2025, **129**, 1495–1505.

180 J. Hubbard and B. H. Flowers, *Proc. R. Soc. London, Ser. A*, 1997, **276**, 238–257.

181 H. Lischka, D. Nachtigallová, A. J. A. Aquino, P. G. Szalay, F. Plasser, F. B. C. Machado and M. Barbatti, *Chem. Rev.*, 2018, **118**, 7293–7361.

17244 | *Phys. Chem. Chem. Phys.*, 2025, **27**, 17225–17244

This journal is © the Owner Societies 2025